

3 **A semi-analytic afterglow with thermal electrons and synchrotron self-Compton emission**

4 DONALD C. WARREN,¹ MARIA DAINOTTI,^{2,3,4} MAXIM V. BARKOV,⁵ BJÖRN AHLGREN,^{1,6} HIROTAKA ITO,⁷
5 AND SHIGEHIRO NAGATAKI^{1,7}

¹*RIKEN Interdisciplinary Theoretical and Mathematical Sciences Program (iTHEMS), Wakō, Saitama, 351-0198 Japan*

²*National Astronomical Observatory of Japan, NAOJ, Mitaka, Tokyo, Japan*

³*The Graduate University for Advanced Studies, SOKENDAI, Shonankokusaimura, Hayama, Miura District, Kanagawa
240-0193, Japan*

⁴*Space Science Institute, 4750 Walnut St, Suite 205, Boulder, CO, 80301, USA*

⁵*Institute of Astronomy, Russian Academy of Sciences, Moscow, 119017 Russia*

⁶*Department of Physics, KTH Royal Institute of Technology, and The Oskar Klein Centre, SE-10691 Stockholm, Sweden*

⁷*RIKEN Cluster for Pioneering Research (CPR), Astrophysical Big Bang Laboratory (ABBL), Wakō, Saitama, 351-0198 Japan*

ABSTRACT

We extend previous work on gamma-ray burst (GRB) afterglows involving hot thermal electrons at the base of a shock-accelerated tail. Using a physically-motivated electron distribution based on first-principles simulations, we compute broadband emission from radio to TeV gamma-rays. For the first time, we present the effects of a thermal distribution of electrons on synchrotron self-Compton (SSC) emission. The presence of thermal electrons causes temporal and spectral structure across the entire observable afterglow, which is substantively different from models that assume a pure power-law distribution for the electrons. We show that early-time TeV emission is enhanced by more than an order of magnitude for our fiducial parameters, with a time-varying spectral index that does not occur for a pure power law of electrons. We further show that the X-ray “closure relations” take a very different, also time-dependent, form when thermal electrons are present; the shape traced out by the X-ray afterglows is a qualitative match to observations of the traditional decay phase.

1. INTRODUCTION

The afterglows of gamma-ray bursts (GRBs) were initially used to localize the hosts, determine redshifts, and conclusively demonstrate the cosmological origin of these events (Costa et al. 1997; van Paradijs et al. 1997; Metzger et al. 1997; Bloom et al. 1998). Even before the first afterglows were observed, however, it was known that broadband observations would allow for the determination of the properties of GRBs and their progenitor systems (e.g., Paczyński & Rhoads 1993). A standard picture of GRB afterglows was developed, which assumed a relativistic shock accelerating electrons into a power-law distribution (Sari et al. 1998; Granot & Sari 2002, and countless others); these electrons then produced, by synchrotron radiation, the photons detected at Earth. Despite the simplicity of the model, it has been fitted with great success to numerous afterglows (Perley et al. 2014; Laskar et al. 2016; Troja et al. 2019).

36 The standard picture of synchrotron afterglows is not without problems, however. Fairly early on it was
 37 realized that not all electrons were necessarily part of the power law producing the radiation; in fact, the
 38 synchrotron model is degenerate with respect to the fraction f_{NT} of non-thermal radiating electrons (Eichler
 39 & Waxman 2005). While certain observations could break the degeneracy (Toma et al. 2008), most authors
 40 assume $f_{\text{NT}} = 1$ on the principle of parsimony. A second issue with the standard afterglow is how to
 41 characterize the electrons that are not part of the power-law tail. Eichler & Waxman (2005) assumed that
 42 they formed a cool, thermal distribution at energies far below the base of the power law. First-principles
 43 simulations of shock formation and particle acceleration later showed that (at least for some part of the
 44 parameter space relevant to GRBs) relativistic shocks produce a hot thermal distribution that is smoothly
 45 connected to the traditional nonthermal population (Sironi & Spitkovsky 2011; Sironi et al. 2013).

46 Various authors have described the effects of a hot thermal electron population on afterglow emission.
 47 Giannios & Spitkovsky (2009) computed light curves and spectral evolution for a variety of mixed (thermal
 48 and nonthermal) distributions, but they used an oversimplified model of emission. In a pair of papers,
 49 Warren et al. (2017, 2018) considered the nonlinear interaction between relativistic shocks and the particle
 50 distributions they produce, as well as the consequences for GRB afterglows. However, their model for
 51 computing emission was also simplified. Ressler & Laskar (2017) produced the most thorough analysis to
 52 date of thermal electrons in GRB afterglows, solving the radiative transfer equation for both synchrotron
 53 emission and absorption within the surface of equal arrival time. Of these studies of thermal electrons, only
 54 Warren et al. (2017) discussed the impact of thermal electrons on TeV emission from GRB afterglows. This
 55 was a largely theoretical concern until GRB 180720B and GRB 190114C, both of which produced photons
 56 above 300 GeV (MAGIC Collaboration et al. 2019; Abdalla et al. 2019).

57 The standard synchrotron afterglow breaks the photon spectrum into a (possibly smoothly connected)
 58 broken power law (Sari et al. 1998; Granot & Sari 2002). It is therefore possible to describe the temporal
 59 ($F_\nu \propto t^{-\alpha}$) and spectral ($F_\nu \propto \nu^{-\beta}$) behavior for any desired frequency band or observer time. One can then
 60 compute the so-called ‘‘closure relations’’, which relate α and β for the afterglow. Numerous works have
 61 computed these closure relations under a wide variety of physical conditions (wind-like or constant-density
 62 ambient medium, slow- or fast-cooling electrons, presence or absence of a reverse shock, etc. Sari et al.
 63 1998; Zhang & Mészáros 2004; Racusin et al. 2009; Gao et al. 2013; Ryan et al. 2020). Other authors have
 64 applied closure relations to populations of GRBs in order to interpret observations of the standard afterglow
 65 decay phase to pinpoint a statistically favored GRB scenario (Srinivasaragavan et al. 2020); or applied the
 66 same procedure to the shallower plateau emission phase (Dainotti et al. 2021a). Closure relations have
 67 additionally been used in an attempt to identify the afterglow environment of select peculiar GRBs (such as
 68 those with a plateau in both their GeV and X-ray light curve: Dainotti et al. 2021b).

69 The aim of this paper is to extend prior work on thermal electrons in GRB afterglows, especially their
 70 relevance to observable TeV emission. In Section 2 we outline a semi-analytical description of a GRB
 71 afterglow with hot thermal electrons. In Section 3 we define the two main models used in this work, as well
 72 as discussing the mostly-free parameter f_{NT} . We solve the radiative transfer equation and present broadband
 73 spectra in Section 4. In Section 5 we discuss the effects of thermal electrons on light curves, spectral and
 74 temporal indices. We then interpret the joint behavior of the indices, as applied to X-ray closure relations,
 75 in Section 6. We conclude in Section 7.

2. MODEL

The model presented here may be conceptually divided into four parts: (1) a description of the hydrodynamic properties of the forward shock responsible for the afterglow; (2) formulae governing the initial electron distribution as it decouples from the shock and ceases to be accelerated; (3) photon production and absorption processes; and (4) a method of integrating flux from every location in the observable afterglow. Several of these components have been presented in the literature previously (Granot & Sari 2002; Ressler & Laskar 2017) but we repeat them here for completeness.

The parameters needed for the model are those commonly used in the study of GRB afterglows. The hydrodynamics of the jet are decided by the isotropic kinetic energy E_{iso} and the external density. This density, $n_{\text{ext}}(R) = AR^{-k}$, may depend on the distance from the central engine. The choices $k = 0$ for a constant-density ambient medium and $k = 2$ for a wind-like ambient medium are typical. Whichever value of k is used, the parameter A sets the number density of protons being encountered by the forward shock; for $k = 0$, $A \equiv n_{\text{ISM}} \text{ cm}^{-3}$, while for $k = 2$, $A \equiv A_{\star} \text{ cm}^{-1}$. Four parameters control the microphysics of the electron distribution and photon production. The parameters ϵ_e and ϵ_B are the fractions of inflowing kinetic energy placed in electrons and magnetic fields, respectively.¹ The third microphysical parameter p governs the steepness of the shock-accelerated electron distribution, i.e. $dN/dE \propto E^{-p}$. Finally, the fraction of electrons that are injected into the shock-acceleration process, and thus the fraction of electrons that form the non-thermal distribution, is controlled by the parameter f_{NT} .

Since these bursts occur at cosmological distances, our calculations use the redshift z to the GRB. In converting this to a luminosity distance we assume a flat Universe with $H_0 = 67.7 \text{ km s}^{-1} \text{ Mpc}^{-1}$, $\Omega_m = 0.311$, and $\Omega_{\Lambda} = 1 - \Omega_m$ (Wright 2006; Planck Collaboration et al. 2020).

We make two further assumptions. First of these is that the blast wave is assumed to be spherical: we do not consider the angular extent of the jet, nor any angular structure. We cannot therefore discuss effects like a jet break, or the relationship between viewing angle and observations. The second assumption is that we do not include a reverse shock in our model. The physical state of the GRB ejecta, through which the reverse shock propagates, is far less certain than the physical state of the ambient medium. As such the reverse shock is much less clearly defined than is the forward shock. Including a reverse shock would mean the addition of new parameters beyond those listed in the previous paragraphs (Zhang & Kobayashi 2005; Japelj et al. 2014; Barkov et al. 2021). Both the angular structure of the blast wave and any reverse shock are complications which we defer to future work.

2.1. Hydrodynamics

Since we assume a spherically-symmetric burst, the bulk motion of the fluid is governed by the self-similar solution of Blandford & McKee (1976),

$$E_{\text{iso}} = \frac{8\pi A m_p c^2 \Gamma^2 R^{3-k}}{17 - 4k}, \quad (1)$$

¹ The remaining kinetic energy is placed in protons, such that $\epsilon_e + \epsilon_B + \epsilon_p = 1$. Since protons are not significant contributors to photon production or absorption, we do not discuss them further in this work.

109 for an adiabatic blast wave with a shock Lorentz factor Γ at a distance R from the central engine. The radius
 110 of the shock is related to the time since the burst (in the rest frame of the progenitor) by

$$R = ct \left(1 - \frac{1}{2(4-k)\Gamma^2} \right), \quad (2)$$

111 and the radial location of points in the GRB interior may be expressed using the similarity variable

$$\chi = 1 + 2(4-k)\Gamma^2 \left(\frac{R-r}{R} \right). \quad (3)$$

112 In Equation 3, and elsewhere in the paper, we use R to refer to points on the forward shock (where $\chi = 1$)
 113 and r to refer to points in the interior of the blast wave (where $\chi > 1$). The similarity variable χ also relates
 114 the current state of the blast wave to the state at which a particular fluid parcel initially crossed the shock:

$$\chi = \left(\frac{R}{R_0} \right)^{4-k}, \quad (4)$$

115 where R_0 is the shock radius when $\chi = 1$ for the fluid under consideration.

116 The [Blandford & McKee \(1976\)](#) solution provides formulae for the proper energy density e , proper
 117 number density n , and the fluid Lorentz factor γ in the progenitor rest frame:

$$\begin{aligned} e &= 2\Gamma^2 A m_p c^2 \chi^{-(17-4k)/3(4-k)} \\ n &= 2^{3/2} \Gamma A \chi^{-(10-3k)/2(4-k)} \\ \gamma &= 2^{-1/2} \Gamma \chi^{-1/2} \end{aligned} \quad (5)$$

118 We reserve Γ for the Lorentz factor of the forward shock, and use γ for the bulk motion of fluid. As needed,
 119 the local magnetic field strength is computed using the equipartition parameter ε_B ,

$$B^2 = 8\pi\varepsilon_B e. \quad (6)$$

120 Note the assumption that ε_B is uniform in space and constant in time. It is expected from PIC simulations
 121 that there will be short-wavelength magnetic field turbulence at the forward shock, and that this turbulence
 122 can lead to detectable observational signatures ([Lemoine 2013](#); [Lemoine et al. 2013](#)). At present we ignore
 123 this complication.

124 2.2. Electron distribution

125 Rather than use PIC simulations (e.g., [Sironi et al. 2013](#)) or Monte-Carlo simulations (e.g., [Warren et al.](#)
 126 [2017](#)) to determine the distributions of radiating particles, we define the distributions analytically based on
 127 the shock conditions when particles first encountered the blast wave, and on the history of the fluid post-
 128 shock. We also track the evolution of the distributions as they advect away from the forward shock of the
 129 blast wave.

2.2.1. *The initial distribution*

130

131 As we are using a mixed distribution featuring both a thermal population and a non-thermal tail, we use
 132 four quantities to set the initial state of the distributions: (1) the location of the thermal peak; (2) the spectral
 133 index of the non-thermal tail; (3) the maximum energy, above which radiative losses exceed acceleration
 134 gains; and (4) the crossover point between the thermal peak and the non-thermal tail. Since we consider
 135 only leptonic emission processes (see Section 2.3), we need only discuss the electron distributions.

136 The thermal component of the electron distribution function is given by the Maxwell–Jüttner distribution
 137 in momentum,

$$\frac{dn_{e,\text{TH}}}{d\gamma_e} = C_{\text{TH}}\gamma_e^2\beta_e e^{-\frac{\gamma_e}{a}}, \quad (7)$$

138 where γ_e is the electron Lorentz factor in the plasma rest frame, and $\beta_e = \sqrt{1 - \gamma_e^{-2}}$. PIC simulations show
 139 that the thermal peak of the electron distribution lies at an energy $E = \epsilon_e\Gamma m_p c^2 \gg m_e c^2$, from which we get
 140 the parameter a in Equation 7:

$$a = \frac{\epsilon_e\Gamma m_p}{3m_e}, \quad (8)$$

141 the factor of 3 being necessary so that the average over the entire Maxwell–Jüttner distribution yields the
 142 desired value.

143 The non-thermal tail of the electron distributions is characterized by a fixed spectral index p and a max-
 144 imum Lorentz factor $\gamma_{e,\text{max}}$:

$$\frac{dn_{e,\text{NT}}}{d\gamma_e} = C_{\text{NT}}\gamma_e^{-p} e^{-(\gamma_e/\gamma_{e,\text{max}})^2}. \quad (9)$$

145 The maximum energy of the tail depends on the microphysics of shock acceleration and the strength of the
 146 radiative cooling. We employ the empirical broken power law formula found in Warren et al. (2021) for the
 147 maximum electron energy as a function of proper shock speed $\Gamma\beta$,

$$\gamma_{e,\text{max}}(\Gamma\beta) = \gamma_{e,\text{pk}} \left(\frac{\Gamma\beta}{\Gamma_{\text{pk}}\beta_{\text{pk}}} \right)^L \left[\frac{1 + \frac{L}{H}}{1 + \left(\frac{L}{H}\right) \left(\frac{\Gamma\beta}{\Gamma_{\text{pk}}\beta_{\text{pk}}}\right)} \right]^{\frac{L+H}{W}}. \quad (10)$$

148 This formula was derived from Monte Carlo simulations of electron acceleration and cooling in a micro-
 149 turbulent magnetic field, and so is well-suited for describing the electron distributions of GRB afterglows.
 150 Equation 10 is controlled by five features,

$$\begin{aligned} \gamma_{e,\text{pk}} &= 6.35 \times 10^5 (m_p/m_e) \\ \Gamma_{\text{pk}}\beta_{\text{pk}} &= 0.532 (\epsilon_B n_{\text{ext}})^{-0.338} \\ L &= 2.12 \\ H &= 1.01 \\ W &= 5.26 (\epsilon_B n_{\text{ext}})^{0.11}. \end{aligned} \quad (11)$$

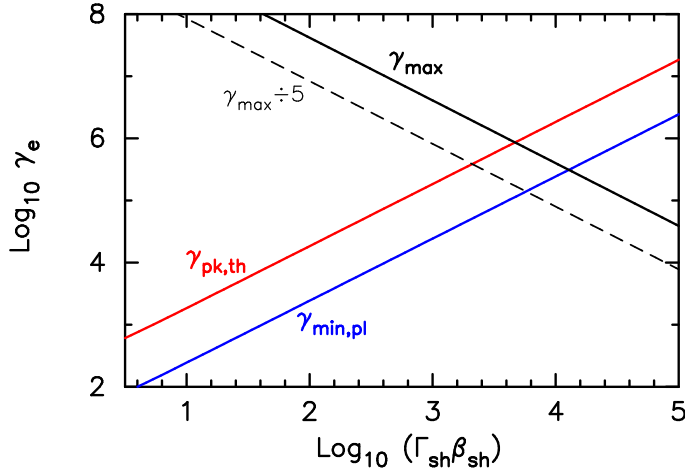


Figure 1. Key electron Lorentz factors as a function of the forward shock proper speed. The red line is the location of the thermal distribution peak (Equation 8), and the blue line is the minimum electron Lorentz factor for a pure power law. The solid black line is the maximum electron Lorentz factor predicted by Equation 10. The light, dashed black line below that is the same quantity, but shifted downward by a factor of 5. All three electron Lorentz factors depend on the parameters of the GRB, which we list in Table 2.

151 Briefly, the five features are: (1) $\gamma_{e,\text{pk}}$, the Lorentz factor at the peak of the broken power law; (2) $\Gamma_{\text{pk}}\beta_{\text{pk}}$, the
 152 value of $\Gamma\beta$ at which the peak occurs; (3,4) L (H), the power-law behavior of Equation 10 below (above)
 153 the peak; and (5) W , the width of the break.² The physical meanings of these features, and their numerical
 154 values, are discussed at greater length in Warren et al. (2021).

155 Using the Blandford–McKee solution with the Warren et al. (2021) maximum electron energy presents
 156 a problem. The Blandford–McKee solution allows for arbitrarily large shock Lorentz factors, particularly
 157 at early times or for particles deep within the “egg”. Since the maximum electron energy is a decreasing
 158 function of Lorentz factor when $\Gamma \gg 1$, and the minimum electron energy is an increasing function of Γ , the
 159 model can predict electron distributions where the minimum energy is greater than the maximum energy.

160 The situation is illustrated in Figure 1. The red and blue lines show possible “minimum” Lorentz factors
 161 for a nonthermal, shock-accelerated electron distribution: either the location of the thermal peak (in red), or
 162 the base of the power law when no thermal peak is present (in blue). The thicker black line is the maximum
 163 electron Lorentz factor given by Equation 10. For sufficiently large shock speeds the maximum value of
 164 the shock-accelerated tail can be less than either plausible minimum value. In order to cleanly separate the
 165 thermal peak from the nonthermal tail, one needs $\gamma_{e,\text{max}} \gtrsim 5\gamma_{e,\text{th,pk}}$ (see Figure 2). This even more restrictive
 166 scenario is shown by the light dashed line in Figure 1. The interpretation of such situations, where the
 167 maximum energy attainable by shock acceleration is less than (or close to) the energy of the thermal peak, is
 168 that no acceleration is possible (or that the accelerated population cannot be adequately distinguished from
 169 the thermal distribution). If $\gamma_{e,\text{max}} \ll \gamma_{e,\text{th,pk}}$, one might even expect the inflowing electrons to significantly
 170 cool as they are heated by the microturbulent field, in which case the downstream electron distribution would
 171 no longer be thermal in nature.

²The values presented in Equation 11 assume very efficient shock acceleration. Specifically, we have assumed Bohm-like diffusion, in which the electrons’ mean free path through the magnetic field turbulence is equal to their gyroradius: $\lambda_{\text{mfpl}} = \eta_{\text{mfpl}} r_g$, with $\eta_{\text{mfpl}} = 1$. If η_{mfpl} were greater than 1, the maximum energy would be lower since electrons would generally spend more time completing each shock crossing cycle.

172 In physical GRBs, however, the forward shock may not have arbitrarily large Lorentz factors. It is
 173 generally held that a “coasting” phase takes place before deceleration begins, which would serve as an upper
 174 bound on the shock Lorentz factors used in our model (Meszaros et al. 1993; Kobayashi et al. 1999). We
 175 use a coasting Lorentz factor $\eta = 1000$ here, which is a plausible (if a bit high) upper limit and places $\gamma_{e,\max}$
 176 well above the location of the thermal peak.

177 The final piece of the initial electron distribution is the crossover Lorentz factor γ_\times , where we stop using
 178 Equation 7 and start using Equation 9. We calculate this in a manner similar to Giannios & Spitkovsky
 179 (2009) and (Ressler & Laskar 2017) (see also Kafexhiu et al. 2019): set the two equations to have an equal
 180 value at some electron energy, set their relative normalizations using the parameter f_{NT} , and set the total
 181 normalization of the combined distribution to the proper density (Equation 5). The three constraints are

$$\begin{aligned} n(1 - f_{\text{NT}}) &= \int_1^{\gamma_\times} C_{\text{TH}} \gamma_e^2 \beta_e e^{-\frac{\gamma_e}{a}} d\gamma_e, \\ n f_{\text{NT}} &= \int_{\gamma_\times}^{\infty} C_{\text{NT}} \gamma_e^{-p} e^{-(\gamma_e/\gamma_{e,\max})^2} d\gamma_e, \end{aligned}$$

182 and

$$C_{\text{NT}} \gamma_\times^{-p} e^{-(\gamma_\times/\gamma_{e,\max})^2} = C_{\text{TH}} \gamma_\times^2 \beta_\times e^{-\frac{\gamma_\times}{a}}. \quad (12)$$

183 These three equations are solved numerically as needed, and provide not only the crossover energy γ_\times but
 184 also the two normalization constants. That is, given n , f_{NT} , a , and $\gamma_{e,\max}$ we compute γ_\times , which in turn allows
 185 us to find C_{TH} and C_{NT} and evaluate Equations 7 and 9.

186 Note that if no thermal electrons are present, the electron distribution is defined by the pure power law
 187 of Equation 9. In such a situation the value of C_{NT} is fixed by the normalization condition,

$$C_{\text{NT}} = n(p-1) \gamma_{\min}^{p-1} \quad (13)$$

188 where

$$\gamma_{\min} = \frac{(p-2)\epsilon_e \Gamma m_p}{\sqrt{2}(p-1)m_e} \quad (14)$$

189 is the minimum electron Lorentz factor in the power law. It is worth pointing out that Equation 14 allows
 190 for γ_{\min} values less than unity, if p is approximately 2 and Γ is not extremely large. Care must be taken when
 191 applying this equation to ensure that one is not in regions of the parameter space where such an unphysical
 192 outcome can occur. (The issue could be averted by casting Equations 9, 13 and 14 in terms of electron
 193 momentum rather than Lorentz factor.)

2.2.2. Post-shock cooling

195 The above equations define the electron distribution at the time electrons decouple from the shock—
 196 when the thermal electrons cross the shock, and when the shock-accelerated electrons cross the shock for
 197 the final time. As the fluid advects downstream from the shock, the electrons experience both adiabatic and
 198 radiative cooling. The plasma-frame Lorentz factors of the electrons evolve according to

$$\frac{d\gamma_e}{dt'} = -\frac{\sigma_T B^2 \gamma_e^2}{6\pi m_e c} + \frac{\gamma_e}{3n} \frac{dn}{dt'}, \quad (15)$$

199 where the first term represents the radiative losses (with σ_T being the Thomson cross section) and the second
 200 term represents the adiabatic losses.

201 Equation 15 can be rewritten in terms of the Blandford–McKee self-similarity variable χ (for details,
 202 see Granot & Sari 2002). At a location χ within the shock structure, a hypothetical electron with infinite
 203 initial energy will have cooled to

$$\gamma_\infty(\chi) = \frac{2(19 - 2k)\pi m_e^2 c^3 \gamma_0}{\sigma_T B_0^2 t_0} \frac{\chi^{(25-2k)/[6(4-k)]}}{\chi^{(19-2k)/[3(4-k)]} - 1}. \quad (16)$$

204 In this equation B_0 and t_0 are, respectively, the magnetic field and progenitor-frame time at which the elec-
 205 trons began to cool, while γ_0 is the fluid bulk Lorentz factor (not the initial electron Lorentz factor; see
 206 Equation 5) at time t_0 . Note that $\gamma_\infty(\chi)$ is simply an intermediate step in the calculation; since our electron
 207 distribution does not actually extend to infinite energy (being limited to approximately the value shown in
 208 Equation 10) there are never electrons present with this Lorentz factor. Electrons that did not possess infinite
 209 energy at $\chi = 1$ will, at some later time, have cooled to a Lorentz factor given by

$$\gamma_e(\gamma_{e,0}, \chi) = \frac{\gamma_{e,0}}{\chi^{(13-2k)/[6(4-k)]} + \gamma_{e,0}/\gamma_\infty(\chi)}. \quad (17)$$

210 As pointed out in Granot & Sari (2002), the quantity $(dn_e/d\gamma_e)(d\gamma_e/n)$ is conserved as the distributions
 211 evolve. So to compute $dn_e/d\gamma_e$ at arbitrary χ we compute the change in $d\gamma_e$ using Equation 17, then rescale
 212 by a further factor of n/n_0 :

$$\frac{dn_e(\chi)}{d\gamma_e} = \frac{dn_{e,0}}{d\gamma_{e,0}} \frac{d\gamma_{e,0}}{d\gamma_e} \frac{n}{n_0}, \quad (18)$$

213 where the subscript 0 denotes the initial values of the various quantities.

214 2.3. Photon processes

215 We consider three photon processes in this work, all leptonic in nature: synchrotron radiation, syn-
 216 chrotron self-absorption (SSA), and synchrotron self-Compton (SSC). We do not consider hadronic emis-
 217 sion processes (e.g. proton synchrotron or photopion production); these are many orders of magnitude less
 218 efficient than leptonic processes at a given photon energy, unless extreme values for the proton distribution or
 219 bulk fluid properties are assumed (Böttcher & Dermer 1998; Zhang & Mészáros 2001; Warren et al. 2015).

220 Synchrotron radiation is computed using the traditional Rybicki & Lightman (1979) formula,

$$P_\nu(\nu, \gamma) = \frac{\sqrt{3}q^3 B \sin \alpha}{m_e c^2} F\left(\frac{\nu}{\nu_{ch}}\right) \quad (19)$$

221 for an electron radiating in a magnetic field of strength B at a pitch angle α between the magnetic field and
 222 the motion of the electron. The characteristic frequency of such a photon is given by

$$\nu_{ch} = \frac{3\gamma^2 q B \sin \alpha}{4\pi m_e c} \quad (20)$$

223 where γ is the Lorentz factor of the electron in the local rest frame of the plasma. The function $F(x)$ is the
224 usual synchrotron function,

$$F(x) = x \int_x^\infty K_{5/3}(t) dt, \quad (21)$$

225 in which $K_{5/3}$ is the modified Bessel function of the second kind, with order parameter 5/3. To find the total
226 synchrotron power at a particular location, we average the emission over all pitch angles and integrate over
227 the electron distribution:

$$P_{v,\text{syn}} = \int \frac{dn_e(\gamma)}{d\gamma} P_{v,\text{avg}}(v, \gamma) d\gamma \quad (22)$$

228 For low-energy photons, the synchrotron self-absorption (SSA) process can be a significant source of
229 opacity. The absorption coefficient is a function of both the electron distribution and the synchrotron power:

$$\alpha_v = -\frac{1}{8\pi m_e v^2} \int \gamma^2 P_v(v, \gamma) \frac{\partial}{\partial \gamma} \left[\frac{dn_e/d\gamma}{\gamma^2} \right] d\gamma \quad (23)$$

231 When $h\nu \ll \gamma m_e c^2$, the function $P_v(v, \gamma)$ is proportional to $v^{1/3} \gamma^{-2/3}$, and the absorption coefficient can be
232 computed analytically (Granot et al. 1999b; Warren et al. 2018). In the interest of generality we do not make
233 that assumption in this work, using Equation 23 everywhere.

234 The third photon process we consider is SSC emission. We use the procedure outlined in Jones (1968),
235 which includes the Klein-Nishina reduction in scattering cross-section and is built upon the following equa-
236 tion:

$$\frac{d^2 N}{dt d\alpha_{\text{out}}} = \frac{2\pi r_0^2 c}{\alpha_{\text{in}} \gamma_e^2} \left[2q'' \ln q'' + (1 + 2q'')(1 - q'') \right. \\ \left. + \frac{1 - q''}{2} \frac{(4\alpha_{\text{in}} \gamma_e q'')^2}{1 + 4\alpha_{\text{in}} \gamma_e q''} \right], \quad (24)$$

237 where $dN/dt \approx c\sigma$ is the number of electron-photon collisions per unit time, normalized to the ambient
238 photon density. This equation calculates the number of photons produced per second per unit outgoing
239 photon energy (expressed as a ratio of the electron rest mass, i.e. $\alpha_{\text{out}} = E_\gamma/[m_e c^2]$). The photons are
240 assumed to be encountering a monoenergetic beam of electrons with Lorentz factor γ_e , and both α_{out} and
241 γ_e are taken in the plasma rest frame. The prefactor uses the classical electron radius, $r_0 = q^2/[m_e c^2]$; the
242 quantity $q'' = \alpha_{\text{out}}/[4\alpha_{\text{in}} \gamma_e (1 - \alpha_{\text{out}}/\gamma_e)]$ relates the incoming photon energy α_{in} to the outgoing photon energy
243 under consideration.

244 To convert Equation 24 into an SSC power, it is necessary to integrate over both the electron distribution
245 and the number density of synchrotron photons present,

$$P_{v,\text{SSC}} = \frac{hE_{\gamma,\text{out}}}{m_e c^2} \int_1^\infty d\gamma_e \frac{dn_e(\gamma_e)}{d\gamma_e} \int_0^{\alpha_{\text{out}}} d\alpha_{\text{in}} \frac{dn_\gamma(\alpha_{\text{in}})}{d\alpha_{\text{in}}} \frac{d^2 N}{dt d\alpha_{\text{out}}}, \quad (25)$$

246 where the prefactor in front of the integral converts $d^2 N/(dt d\alpha_{\text{out}})$ to dP_v/dv_{out} . Transforming the syn-
247 chrotron P_v given by Equation 22 into the photon density needed above requires an assumption about the

248 size of the scattering region. We assume that the region has a width equal to ds , the size of radiation transfer
 249 step as outlined in the next section. With this assumption, we can relate $P_{v,\text{syn}}$ to $dn_\gamma(v)/dv$,

$$\frac{dn_\gamma(v)}{dv} = P_{v,\text{syn}} \frac{ds}{c \cdot h\nu}, \quad (26)$$

250 giving us everything necessary to compute $P_{v,\text{ssc}}$.

251 2.4. Radiative transfer

252 Radiative transfer is handled largely according to the method presented in [Granot & Sari \(2002\)](#). That
 253 is, we solve the equation for radiative transfer in the rest frame of the GRB central engine:

$$\frac{dI_\nu(v_{\text{GRB}})}{ds} = j_{v,\text{syn}}(v_{\text{GRB}}) + j_{v,\text{ssc}}(v_{\text{GRB}}) - \alpha_\nu(v_{\text{GRB}}) I_\nu(v_{\text{GRB}}). \quad (27)$$

254 The quantities $j_{v,\text{syn}}$ and $j_{v,\text{ssc}}$ are related to Equations 22 and 25, respectively, by $j_\nu = P_\nu/(4\pi)$, and must
 255 be computed in the plasma rest frame where emission occurs. We use the Lorentz-invariant products j_ν/v^2
 256 and $\nu\alpha_\nu$ to express Equation 27 in terms of plasma-frame quantities,

$$\frac{dI_\nu(v_{\text{GRB}})}{ds} = \mathcal{D}^2 j_\nu(v_{\text{pf}}) - \frac{I_\nu(v_{\text{GRB}}) \alpha_\nu(v_{\text{pf}})}{\mathcal{D}} \quad (28)$$

257 where $\nu_{\text{pf}} = \nu_{\text{Earth}}(1+z)/\mathcal{D}$ is the plasma-frame photon frequency corresponding to ν_{Earth} at Earth; the
 258 Doppler factor³ $\mathcal{D} = [\gamma(1-\mu\beta)]^{-1}$ relates the plasma rest frame to the rest frame of the GRB progenitor;
 259 and the factor of $(1+z)$ transforms frequencies from the Earth frame to the GRB rest frame, such that
 260 $\nu_{\text{GRB}} = \nu_{\text{Earth}}(1+z)$. Equation 28 must be integrated along lines of sight through the entire volume emitting
 261 radiation observable at a time t_{obs} , a shape called the ‘‘egg’’ in [Granot et al. \(1999a\)](#). For a fuller discussion,
 262 see that paper, [Granot et al. \(1999b\)](#), or especially [Granot & Sari \(2002\)](#). Briefly, though, the shape is limited
 263 by the angle between a fluid parcel’s position and the line of sight, as well as by the size and speed of the
 264 forward shock at any particular observer time:

$$R(\mu) = \frac{ct_{\text{obs}}/(1+z)}{1-\mu + [2(4-k)\Gamma(\mu)^2]^{-1}}. \quad (29)$$

265 When R and Γ are related by the Blandford–McKee solution, Equation 29 traces out an ovoid shape similar
 266 to its namesake. The maximum perpendicular extent of the egg (that is, its angular size in the sky) varies as
 267 the shock decelerates, and is given by

$$R_{\perp,\text{max}} = (5-k)^{(k-5)/[2(4-k)]} \frac{R_{\text{axis}}}{\Gamma_{\text{axis}}}, \quad (30)$$

268 where the subscripts on the right hand side denote quantities taken with $\mu = 1$. To find the total emission at
 269 Earth, we integrate over the solid angle subtended by the egg. Since we are assuming a spherical explosion

³ As in Section 2.1, γ and β here refer to the fluid’s bulk Lorentz factor and speed rather than to an individual particle’s properties.

270 and therefore azimuthal symmetry, it is convenient to recast the angular integral in terms of $x \equiv R_{\perp}/R_{\perp,\max}$,
 271 leading to

$$F_{\nu}(v_{\text{Earth}}) = 2\pi(1+z) \left(\frac{R_{\perp,\max}(t_{\text{obs}})}{d_L} \right)^2 \int_0^1 x I_{\nu}(v_{\text{GRB}}) dx. \quad (31)$$

272 Although we compute SSA in evaluating Equation 31, this is the only absorption process we consider.
 273 SEDs presented in the remainder of this work ignore absorption due to the extragalactic background light
 274 (EBL), extinction due to gas and dust between the GRB and Earth, and other sources.

275 3. CHOOSING f_{NT}

276 For the rest of this paper we discuss two realizations of the electron distribution. The ‘‘PPL’’ model
 277 assumes that all electrons fall into a power-law distribution (Equations 9, 13, 14), and is the traditional
 278 assumption for the study of GRB afterglows. The ‘‘ThPL’’ model uses the mixed thermal and nonthermal
 279 distribution described in Section 2.2. Both the ThPL and PPL models use the same GRB parameters, and
 280 both distributions are normalized to the same local number density (which depends only on the hydrody-
 281 namic evolution and is not model-dependent).

282 The parameter f_{NT} characterizes our ignorance of the actual microphysics present in and around turbulent
 283 relativistic shocks. There is no theoretical lower limit on f_{NT} (besides the obvious $f_{\text{NT}} \geq 0$), but there is a
 284 mathematical upper limit. If γ_{\times} falls below the thermal peak, then the combined distribution appears as a
 285 broken power law: rising until γ_{\times} , and falling afterward. A simple computation (presented in Appendix C
 286 and confirmed by Equation (17) in [Ressler & Laskar 2017](#)) leads to $f_{\text{NT,max}} = 3/(p+2)$. When $p \approx 2.2\text{--}2.5$ as
 287 is traditionally assumed, $f_{\text{NT,max}} \approx 0.7$; this value is far larger than any suggested by a physically-motivated
 288 model for particle acceleration, and is therefore merely a curiosity rather than a useful limitation on an
 289 uncertain parameter.

290 The so-called ‘‘thermal leakage’’ model (e.g., [Ellison 1985](#); [Ellison et al. 2013](#); [Warren et al. 2018](#)) pre-
 291 dicted particle injection at rates $\gtrsim 10\%$.⁴ On the other hand, PIC simulations of relativistic shock formation
 292 and particle injection predict much smaller injection rates, $\sim 1\text{--}3\%$ ([Sironi et al. 2013, 2015](#)), for shocks
 293 propagating into an unmagnetized medium. Shocks encountering a magnetized medium inject fewer parti-
 294 cles still, down to and including $f_{\text{NT}} \approx 0$ for sufficiently strong upstream magnetic fields in the proper
 295 orientation ([Sironi & Spitkovsky 2011](#); [Sironi et al. 2013](#)).

296 Despite the wide range of f_{NT} allowed by PIC simulations, and the even larger range if one includes the
 297 thermal leakage model for electron injection, there is a natural choice if one wishes to determine the effects of
 298 a thermal population of electrons. That choice, as applied previously in [Ressler & Laskar \(2017\)](#), is to align
 299 the nonthermal portion of the ThPL distribution with the PPL distribution. This is not a physically-motivated
 300 choice: ideally one would choose f_{NT} based on the results of PIC simulations or analytic calculations specific
 301 to the shock speed and magnetic field structure. The assumption we make here is entirely ad hoc; it is
 302 chosen to maximize the similarity between ThPL and PPL distributions rather than being based on more
 303 fundamental calculations.

⁴ The plasma downstream from a strong relativistic shock recedes at speed of $c/3$; any particle whose parallel velocity component (i.e. along the shock normal) exceeds this value can counter its advection with the plasma and re-cross the shock if it is traveling upstream. For a totally isotropic distribution of particles with speed $\approx c$, roughly 30% of the particles satisfy this condition, and thus can enter the Fermi acceleration process.

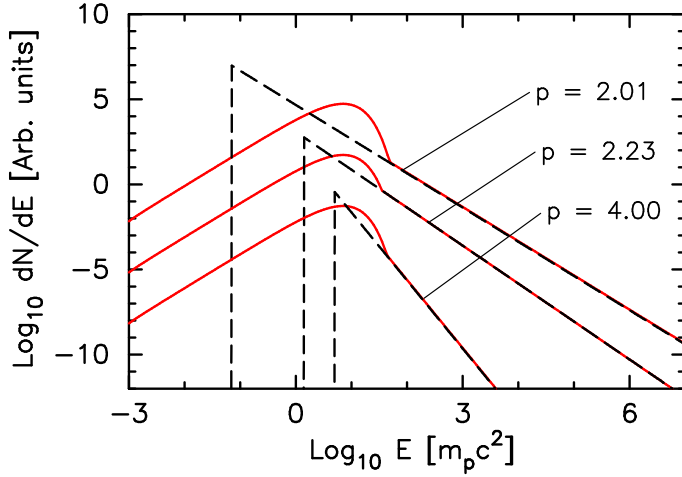


Figure 2. Electron distributions dN/dE as functions of electron energy. Dashed black lines show a pure power-law distribution with the specified index p . Solid red lines show mixed thermal and nonthermal spectra, with f_{NT} set so the nonthermal parts of the spectra overlap. All spectra were calculated for a shock with $\Gamma_0 = 100$ and $\varepsilon_e = 0.1$, and a normalization of 1 cm^{-3} ; distributions were then scaled to enhance readability.

304 We present in Figure 2 several examples of electron distributions. All distributions were computed
 305 using the same values of Γ_0 , ε_e , and total normalization. The sole free parameter was the fraction f_{NT} of
 306 the distribution in the nonthermal tail, which was set so that the PPL distribution overlapped the nonthermal
 307 portion of the ThPL distribution. It is evident from the figure that the two kinds of electron distributions
 308 have maxima at different locations, and that this difference depends on p . It can also be seen in the figure
 309 that the “critical” value of f_{NT} required for overlap depends on p , as nonthermal particles make up a larger
 310 fraction of the overall distribution when $p = 2.23$ than they do in either of the other two cases ($p = 2.01$ and
 311 $p = 4$).

312 One can solve for $f_{\text{NT,crit}}$ by applying a fourth constraint to the system listed in Equation 12. The value
 313 of the power-law portion of the ThPL distribution must match the value of the PPL distribution at γ_x , which
 314 sets C_{NT} to the value given in Equations 13 and 14. Since $\gamma_x \ll \gamma_{e,\text{max}}$, the exponential rollover in the power
 315 laws may be neglected, simplifying the equations considerably. The four equations ultimately reduce to the
 316 following transcendental equation,

$$2e^\delta - 2 - 2\delta - \delta^2 = \frac{1 - f_{\text{NT,crit}}}{(p - 1)f_{\text{NT,crit}}} \delta^3 \quad (32)$$

317 (compare Equation (17) in [Ressler & Laskar 2017](#)) with δ defined as follows:

$$\delta(f_{\text{NT,crit}}) \equiv \frac{\gamma_x}{a} = \frac{3}{\sqrt{2}} \frac{(p - 2)}{(p - 1)} f_{\text{NT,crit}}^{1/(1-p)} \quad (33)$$

318 Figure 3 shows the solutions to Equation 32 over a range of p with astrophysical relevance. Selected
 319 points are listed for reference in Table 1. Both the figure and the table show a trend where $f_{\text{NT,crit}}$ is small
 320 for $p \approx 2$ and $p \gtrsim 4$, with an apparent peak around $p \approx 2.3$. When $p \rightarrow 2$ the base of the power law, E_{min} ,
 321 goes to zero. When p is large, the spectrum drops off so steeply that the portion lying between E_{min} and

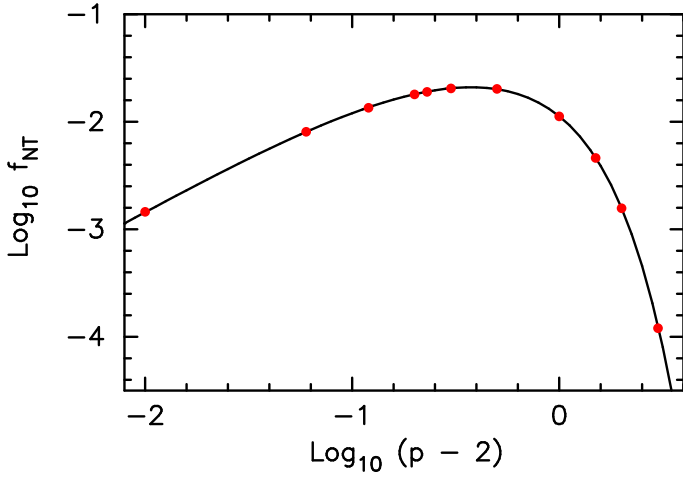


Figure 3. Value of f_{NT} required for overlap in Figure 2, as a function of nonthermal index p . The red dots are taken from Table 1, while the black curve is the solutions to Equation 32.

322 E_{\times} (refer back to Equation 12) is an increasing fraction of the power law's normalization. In both limits the
 323 portion of the power law above E_{\times} is expected to decrease, and this expectation is borne out by the data.
 324 We note also that $f_{\text{NT,crit}}$ is independent of the shock Lorentz factor Γ and the electron equipartition factor
 325 ϵ_e . Since the values of both E_{min} and the thermal peak depend in the same way on Γ and ϵ_e , changing either
 326 parameter merely shifts the curves in Figure 2 left or right; it does not affect the location of the intersection
 327 point relative to either distribution's maximum, and therefore the value of $f_{\text{NT,crit}}$ is also unaffected.

| p | $f_{\text{NT,crit}}$ |
|------|-----------------------|
| 2.01 | 1.44×10^{-3} |
| 2.06 | 8.06×10^{-3} |
| 2.12 | 1.37×10^{-2} |
| 2.20 | 1.76×10^{-2} |
| 2.23 | 1.90×10^{-2} |
| 2.30 | 2.12×10^{-2} |
| 2.50 | 1.97×10^{-2} |
| 3.00 | 1.06×10^{-2} |
| 3.50 | 4.87×10^{-3} |
| 4.00 | 1.54×10^{-3} |
| 5.00 | 1.12×10^{-4} |

Table 1. Normalization constant $f_{\text{NT,crit}}$ associated with each spectral index p .

328 Given the many orders of magnitude spanned by f_{NT} in PIC simulations, it is rather unexpected that the
 329 predictions for unmagnetized shocks ($\sim 1 - 3\%$) align so closely with the values listed in Table 1 for typical
 330 shock-accelerated distributions with $p \approx 2.2$. The coincidence is all the more striking because Table 1 relied
 331 on the unphysical assumption of simply matching non-thermal populations with and without a thermal peak
 332 present.

4. SSC AND SSA WITH THE FULL DISTRIBUTION

Here, and for the rest of the paper, we choose a fiducial set of GRB parameters to compute the evolution of the afterglow. These values are $E_{\text{iso}} = 10^{52}$ erg, $k = 0$, $A = n_{\text{ism}} = 1 \text{ cm}^{-3}$, $\epsilon_e = 0.1$, $\epsilon_B = 0.01$, and $p = 2.23$. When discussing the ThPL model, the parameter f_{NT} is set equal to 0.019, for reasons we elaborated on in Section 3. The maximum Lorentz factor attained by the GRB forward shock is $\eta = 1000$. The burst is assumed to take place at a redshift $z = 1$. The full set of fiducial parameters is listed in Table 2. We require that $\Gamma > 2.5$ everywhere since the Blandford–McKee solution ceases to be an adequate description of the hydrodynamics at lower shock Lorentz factors (Kobayashi et al. 1999); for the above parameters, the latest observer time we can reasonably discuss is $t_{\text{obs}} \approx 1.2 \times 10^6 \text{ s}$.⁵

| Parameter | Value |
|-----------------------------------|---|
| E_{iso} | 10^{52} erg |
| k | 0 |
| $A (= n_{\text{ism}})$ | 1 cm^{-3} |
| ϵ_e | 0.1 |
| ϵ_B | 0.01 |
| p | 2.23 |
| f_{NT}^a | 1.9×10^{-2} |
| η | 1000 |
| z | 1 |
| H_0 | $67.7 \text{ km s}^{-1} \text{ Mpc}^{-1}$ |
| Ω_m | 0.311 |
| $\Omega_\Lambda (= 1 - \Omega_m)$ | 0.689 |

Table 2. List of input GRB parameters and their fiducial values.

^a See discussion in Section 3.

We now include the full suite of processes discussed in Section 2. In this section we discuss the impacts of SSA and SSC, as well as limiting the maximum electron energy to physically-plausible values. We remind the reader that none of the SEDs presented here include intergalactic absorption due to the EBL.

We first compare SEDs from the ThPL (with thermal particles) and PPL (without thermal particles) models in Figure 4, to illustrate the impact of thermal electrons at virtually every part of the observable spectrum. The ratios of SED pairs are presented in Figure 5, offering further insight into the differences between the two distributions.

There is a substantial difference between the ThPL and PPL distributions (see Figure 2), and this difference unsurprisingly carries over to the photon spectra.

- In the radio, there is some difference between the two models, with the ThPL model showing slightly enhanced emission below \sim GHz frequencies throughout the afterglow. The enhancement would be even greater if we were comparing the ThPL model against the fitting formulae of Granot & Sari

⁵The short-wavelength magnetic field turbulence in GRB afterglows is seeded by plasma instabilities that quench at $\Gamma_0 \sim 10$ (Lemoine & Pelletier 2011). It is possible that the magnetic field properties of the blast wave (and the associated values of ϵ_e and ϵ_B) will change long before the fluid solution ceases to apply. For now, we ignore this likely complication in the interest of simplifying the model.

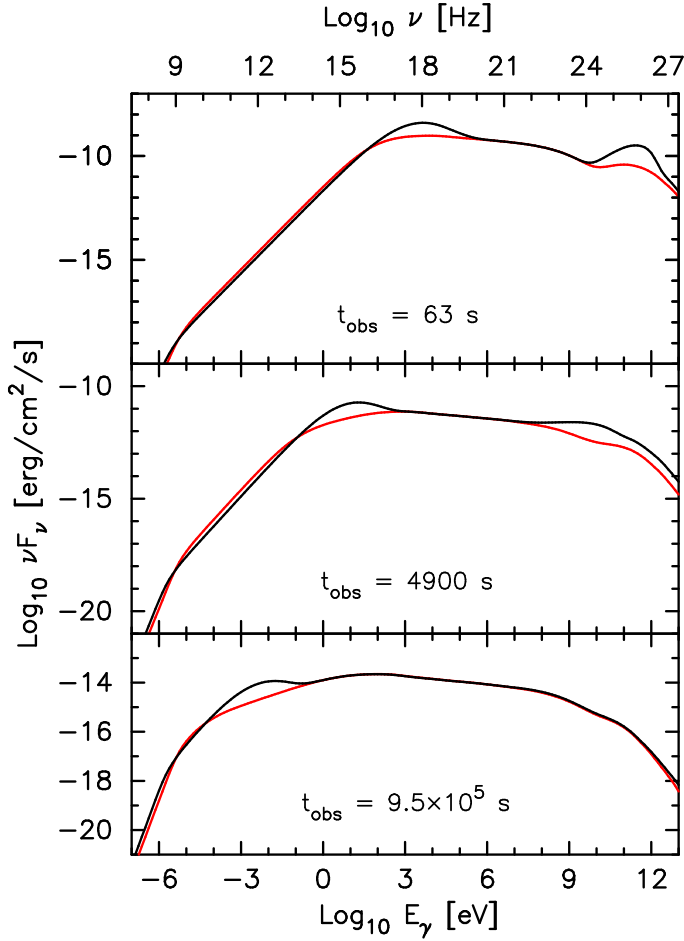


Figure 4. Comparison of SEDs at three observer times, at photon energies from 24 MHz to upwards of 1 TeV. The black line is that of the ThPL model, while the red line is from the PPL model. Note the differing vertical axes for the three subpanels.

356 (2002), due to our correct treatment of SSA and the lower value of v_a here versus there (see Figures 13
357 and 14 in Appendix B).

358 • At photon energies between infrared and X-ray, either of the ThPL or PPL distributions could result in
359 more photon flux. Looking back at Figure 2, PPL electrons outnumber ThPL electrons at the base of
360 the pure power law. At slightly higher electron energies the thermal peak of the ThPL model contains
361 more electrons. This inversion also shows up in the SEDs: as long as the characteristic synchrotron
362 energy of the thermal peak is above any particular waveband, the base of the PPL distribution produces
363 more flux than does the γ_e^2 tail of the thermal electron population. Eventually the thermal peak shifts
364 to low enough energy that its synchrotron flux dominates that of the power law, leading to the obvious
365 peaks in the SEDs at each observer time in Figures 4 and 5.

366 • Recall that f_{NT} was chosen specifically so that the accelerated, nonthermal portion of the ThPL dis-
367 tribution matched the PPL distribution (Section 3). It is to be expected that the SEDs also overlap

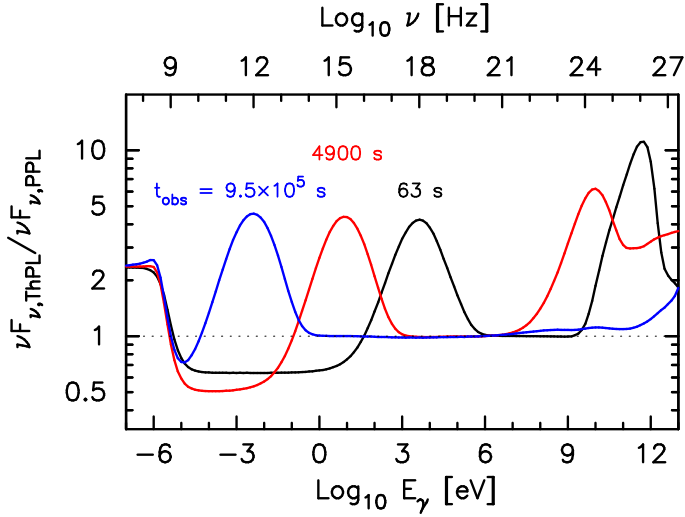


Figure 5. Ratio of the ThPL flux to the PPL flux at the three observer times in Figure 4. The ratios for the three times are plotted in different colors, with black for the SEDs at $t_{\text{obs}} = 63$ s, red for $t_{\text{obs}} = 4900$ s, and blue for $t_{\text{obs}} = 9.5 \times 10^5$ s.

368 above the synchrotron thermal peak, which is indeed the behavior the two models show. For most of
 369 the X-ray afterglow, then, there is not much difference between the two electron distributions.

- 370 • At GeV and TeV energies there is again a very clear difference between the ThPL and PPL SEDs,
 371 due here to the “thermal-thermal” SSC peak: synchrotron photons both produced by, and upscattered
 372 by, thermal electrons. The difference between the two models is upwards of an order of magnitude
 373 early in the afterglow, but it fades with time until there is only marginal enhancement due to thermal
 374 particles. Above ~ 1 TeV the ThPL model is persistently enhanced compared to the PPL model, but
 375 photon fluxes at these energies are already so low—even without EBL absorption considered—that
 376 there is little observational relevance to the distinction.

377 The characterization of the two models at X-ray energies and below agrees qualitatively with prior results,
 378 in particular those of [Ressler & Laskar \(2017\)](#). Differences between our work and theirs are likely due to
 379 how we treated the thermal distribution. While we fixed the energy of our thermal peak and then found γ_{\times}
 380 based on a chosen f_{NT} , [Ressler & Laskar \(2017\)](#) computed γ_{\times} (called $\gamma_{\text{min},0}$ there) first and then fixed the
 382 thermal peak using f_{NT} and γ_{\times} .

383 We now shift our focus away from model comparison and towards a full simulated afterglow using the
 384 ThPL model and the parameters listed in Table 2. In Figure 6 we plot the SEDs for a sequence of times, from
 385 $t_{\text{obs}} = 40$ seconds to $t_{\text{obs}} \approx 11$ days. The figure also shows SEDs due solely to synchrotron emission, i.e.
 386 without SSC. The synchrotron-only curves begin the exponential decay associated with $\gamma_{e,\text{max}}$ (Equation 9) at
 387 about 1 GeV at every observer time computed, which is in excellent agreement with Equation (24) of [Warren](#)
 388 [et al. \(2021\)](#). At the opposite end of the SED, the $F_{\nu} \propto \nu^{1/3}$ segment is visible at all times, confirming that
 389 the afterglow is in the slow-cooling regime from the earliest observer time shown. The transition from fast

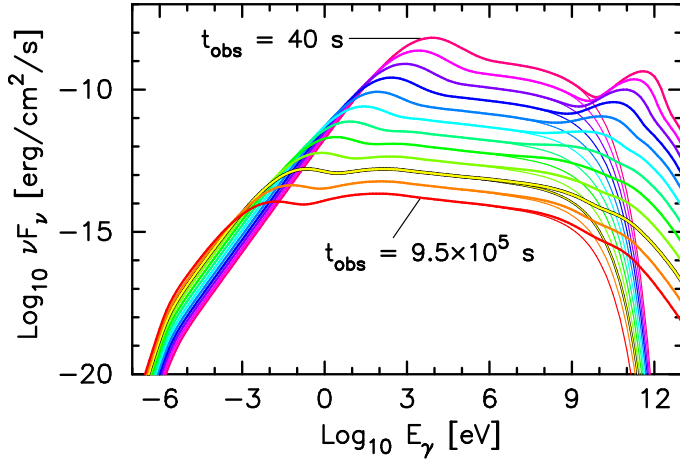


Figure 6. Full SEDs for various times throughout the hypothetical afterglow. The earliest time, in deep pink, is 40 s. Successive SEDs are separated by a factor of 2.5 in observer time, until the red line at $t_{\text{obs}} = 9.5 \times 10^5$ s. At each time, the thick line traces out the full SED, while the thin line is the contribution of synchrotron radiation.

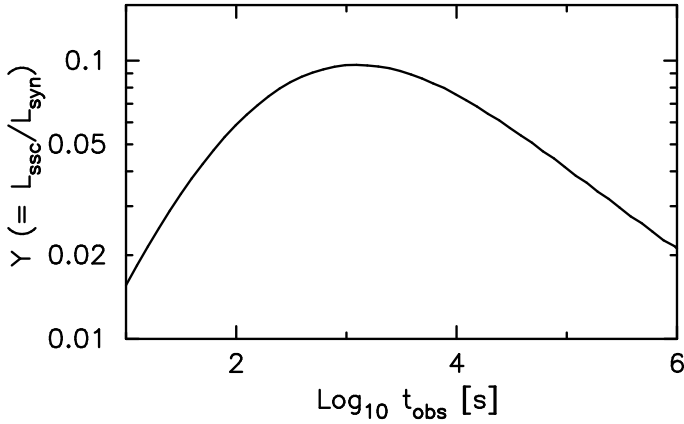


Figure 7. Evolution of the global Compton parameter as a function of observer time.

390 to slow cooling happens at

$$\begin{aligned}
 t_{\text{trans}} &\sim 10^2 \text{ sec} (1+z) \frac{(p-2)^2}{(p-1)^2} \epsilon_{e,-1}^2 \epsilon_{B,-2}^2 n_{\text{ext},0} E_{52} \\
 &\sim 7 \text{ sec}
 \end{aligned}
 \tag{34}$$

391 for our fiducial parameters (Granot & Sari 2002). This is before any observer time presented in Figure 6;
 392 indeed, it is earlier than any observer time considered in this work.

393 The process outlined in Section 2 allows us to compute the Compton Y parameter ($= L_{\text{ssc}}/L_{\text{syn}}$, Sari &
 394 Esin 2001) directly. Not only do we determine $j_{\nu,\text{syn}}$ and $j_{\nu,\text{ssc}}$ locally everywhere in the emitting volume,
 395 but we can use the SEDs in Figure 6 to discuss the global values of $\int F_{\nu,\text{syn}} d\nu$ and $\int F_{\nu,\text{ssc}} d\nu$ and how their
 396 ratio evolves over the course of the simulated afterglow. This ratio is hinted at in Figure 6, but explicitly
 397 presented in Figure 7. At no point in our simulated afterglow does Y exceed, or even approach, unity: the
 398 luminosity due to SSC is a small fraction of the synchrotron luminosity over the entire time considered. The

399 curve in Figure 7 is the global value across the entire shocked region, and it is possible that Y can vary
 400 locally. With that caveat, though, to a first approximation it is reasonable to neglect the backreaction of SSC
 401 on electron cooling (compare against Zacharias & Schlickeiser 2013, for the scenario where Y is too large
 402 to be neglected). This retroactively justifies the assumption made in Warren et al. (2021) to ignore SSC as
 403 a cooling process, for at least some part of the parameter space relevant to GRB afterglows.

404 Since our treatment of SSC in GRB afterglows is a novel extension to the existing literature, we wish
 405 to expand and reiterate on a few points. The effects of the thermal population on SSC are most important
 406 early in the afterglow and at energies above \sim GeV. In this time and energy range, the difference between the
 407 ThPL and PPL models can be more than an order of magnitude even for the parameters listed in Table 2—
 408 which were not chosen for the purpose of maximizing the SSC peaks in Figures 4 and 5. Though we defer
 409 such treatment until future work, one can imagine that there are regions of the parameter space where the
 410 difference between the ThPL and PPL models is even greater in magnitude, or lasts even later into the
 411 afterglow.

412 The synchrotron contribution to the SEDs ends at roughly 1 GeV for all observer times. Given the
 413 steepness of the exponential rolloff, virtually all photons detected above 1 GeV are therefore produced by the
 414 SSC mechanism. This is in line with previous predictions for GeV and TeV emission from GRB afterglows
 415 (Meszaros et al. 1994; Zhang & Mészáros 2001; Liu et al. 2013; Wang et al. 2019; Fraija et al. 2019; MAGIC
 416 Collaboration et al. 2019; Abdalla et al. 2019; Derishev & Piran 2016, 2019). Emission at very high energies
 417 is further enhanced when a thermal distribution of electrons is present, resulting in TeV afterglows that are
 418 (1) brighter at a given observer time, and/or (2) detectable for longer into the afterglow.

419 5. LIGHT CURVES, SPECTRAL AND TEMPORAL INDICES

420 In the previous section we discussed the behavior of multi-wavelength SEDs at individual observer times.
 421 Now we consider the behavior over individual energy ranges and how they evolve with time. Throughout
 422 this, and following, sections, we adopt the convention $F_\nu \propto t^{-\alpha} \nu^{-\beta}$.

423 The light curves at five energies of interest are shown in Figure 8, and we compare the behavior of
 424 afterglows based on the ThPL and PPL models.

- 425 • At radio wavelengths above ν_a the ThPL model is fainter than the PPL model since there are more,
 426 lower-energy, electrons producing unabsorbed synchrotron photons (Figure 2). Our simulation ends
 427 (see discussion in Section 4) as the PPL afterglow peaks in radio, but the ThPL radio afterglow is still
 428 rising. It is a reasonable inference that the late-time behavior of the radio afterglow is similar to that
 429 of the optical afterglow, discussed below.
- 430 • The same initial relation between the ThPL and PPL models is visible in the early optical afterglow. At
 431 $t_{\text{obs}} \approx 300$ s, ν_m for the PPL model passes through the optical and the PPL afterglow begins to decline;
 432 the thermal peak for the ThPL afterglow does not reach optical frequencies until $t_{\text{obs}} \approx 1600$ s, a factor
 433 of 5 later in time. The ThPL afterglow then experiences a period of steep decline, with $\alpha \approx 1.7$ before
 434 optical photons are again produced by the accelerated part of the ThPL distributions. Once this occurs
 435 the ThPL and PPL optical afterglows overlap, as expected from Figures 4 and 5.

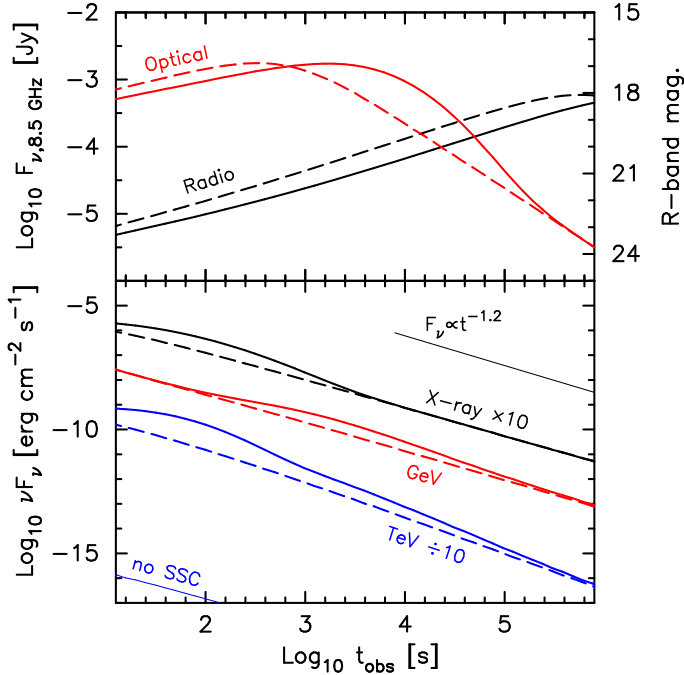


Figure 8. Light curves at five energies. In both panels, solid lines are light curves produced by the ThPL model; dashed lines were computed using the PPL model. *Top panel:* light curves in radio (8.46 GHz; left axis) and optical (640 nm; \sim R-band; right axis). *Bottom panel:* light curves in X-ray (0.3 – 10 keV, *Swift* XRT), GeV (80 – 25000 MeV, *Fermi* LAT), and TeV (300 – 1000 GeV, MAGIC). The X-ray and TeV curves have been scaled for clarity reasons, and the thin line at the bottom left is TeV emission (scaled like the other TeV curve) if SSC is ignored as a photon production process.

- 436 • The ThPL excess in X-rays is due to the thermal synchrotron peak, and vanishes as the spectral feature
437 passes out of the X-ray waveband. The same light curve feature appears in the TeV band as well,
438 and at the same time. The temporal correlation between the light curves in both bands is possibly
439 coincidental, and due to the particular values of the GRB parameters used. It is nonetheless intriguing,
440 and merits further scrutiny as more GRBs are detected in the TeV band. The TeV excess persists for
441 longer than the X-ray excess does, since the thermal electrons of the ThPL distributions (being at
442 higher energies than the base of the PPL distributions) can upscatter photons to TeV energies for
443 longer.
- 444 • The GeV excess is, like the TeV excess, due to thermal-thermal SSC, not to the thermal synchrotron
445 peak. It occurs later than the TeV excess because the thermal-thermal SSC peak takes time to descend
446 in energy to that waveband. It is also less pronounced than either the X-ray or the TeV excesses, since
447 the spectral feature producing it is already decaying by the time that feature reaches GeV energies (see
448 Figure 4).

449 Finally, note in the bottom panel of Figure 8 the thin line labeled “no SSC”. This is the TeV light curve when
450 SSC is ignored as an emission process, and it sits a full six orders of magnitude lower than even the PPL
451 TeV light curve. The fiducial parameters in Table 2 are fairly ordinary for GRBs, so the “no-SSC” curve

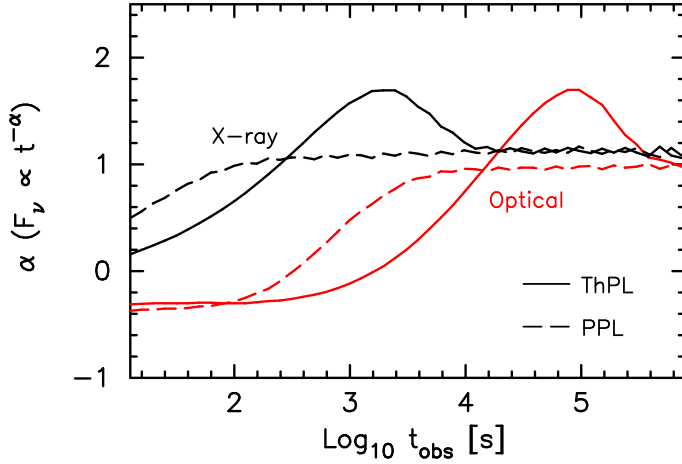


Figure 9. Temporal index α as a function of observer time, in two bands of interest. Black curves show the evolution in the X-ray band (0.3 – 10 keV), and red curves show optical (640 nm; R band). Solid lines show the values associated with the ThPL model, and dashed lines are the values from the PPL model.

452 highlights that extreme values would be needed to close the gap and allow TeV emission to be produced
 453 solely via the synchrotron process.

454 The canonical X-ray afterglow decays with $\alpha \approx 1.2$ (Zhang et al. 2006; Nousek et al. 2006), and we have
 455 drawn a guideline for this decay index in the bottom panel of Figure 8. Both the X-ray and GeV light curves
 456 match this decline, when those photons are coming from the accelerated tail rather than the thermal peak
 457 of the electron distributions. The PPL TeV light curve decays slightly more steeply, with $\alpha \approx 1.4$, and the
 458 ThPL TeV light curve would be steeper still since it spends the majority of the observed afterglow decaying
 459 towards the PPL values.

460 Another feature of the canonical afterglow is a shallow plateau before the $\alpha \approx 1.2$ phase. Figure 8 sug-
 461 gests that it is not possible to create this kind of shallow X-ray decay using just thermal particles. Although
 462 the X-ray light curve does have a shallow decay phase (due to the passage of the synchrotron thermal peak),
 463 it is joined to the $\alpha \approx 1.2$ phase by a steeper decay rather than by a direct transition. The work of Ressler
 464 & Laskar (2017) leads to the same conclusion: a GRB afterglow expanding into a constant-density medium
 465 does not have a shallow plateau smoothly connected to the traditional afterglow phase. A wind-like circum-
 466 burst medium might allow such an X-ray light curve (see Figure (5) of Giannios & Spitkovsky 2009), but
 467 this medium was not considered either here or in Ressler & Laskar (2017).

468 The X-ray behavior described in the previous paragraph is illustrated in Figure 9. The PPL curve shows
 469 the monotonic behavior required to match the canonical X-ray afterglow (although no plateau phase is evi-
 470 dent for the observer times plotted); at early observer times the ThPL curve is flatter (smaller α) than the PPL
 471 curve, after which it steepens to a peak $\alpha \approx 1.7$ and finally relaxes to the PPL value. The behavior is echoed
 472 at optical frequencies, though predictably at later times since the synchrotron peak needs to drop further in
 473 energy. Note, however, that the optical α curves flatten out slightly below the X-ray curves. This is because
 474 the synchrotron cooling break ν_c still lies between the two wavebands at the end of our simulation. If we ran
 475 to later times, ν_c would pass through the optical waveband, and the optical light curve would steepen slightly
 476 to match the X-ray light curve (this same behavior was shown in Figure 8 of Giannios & Spitkovsky 2009).

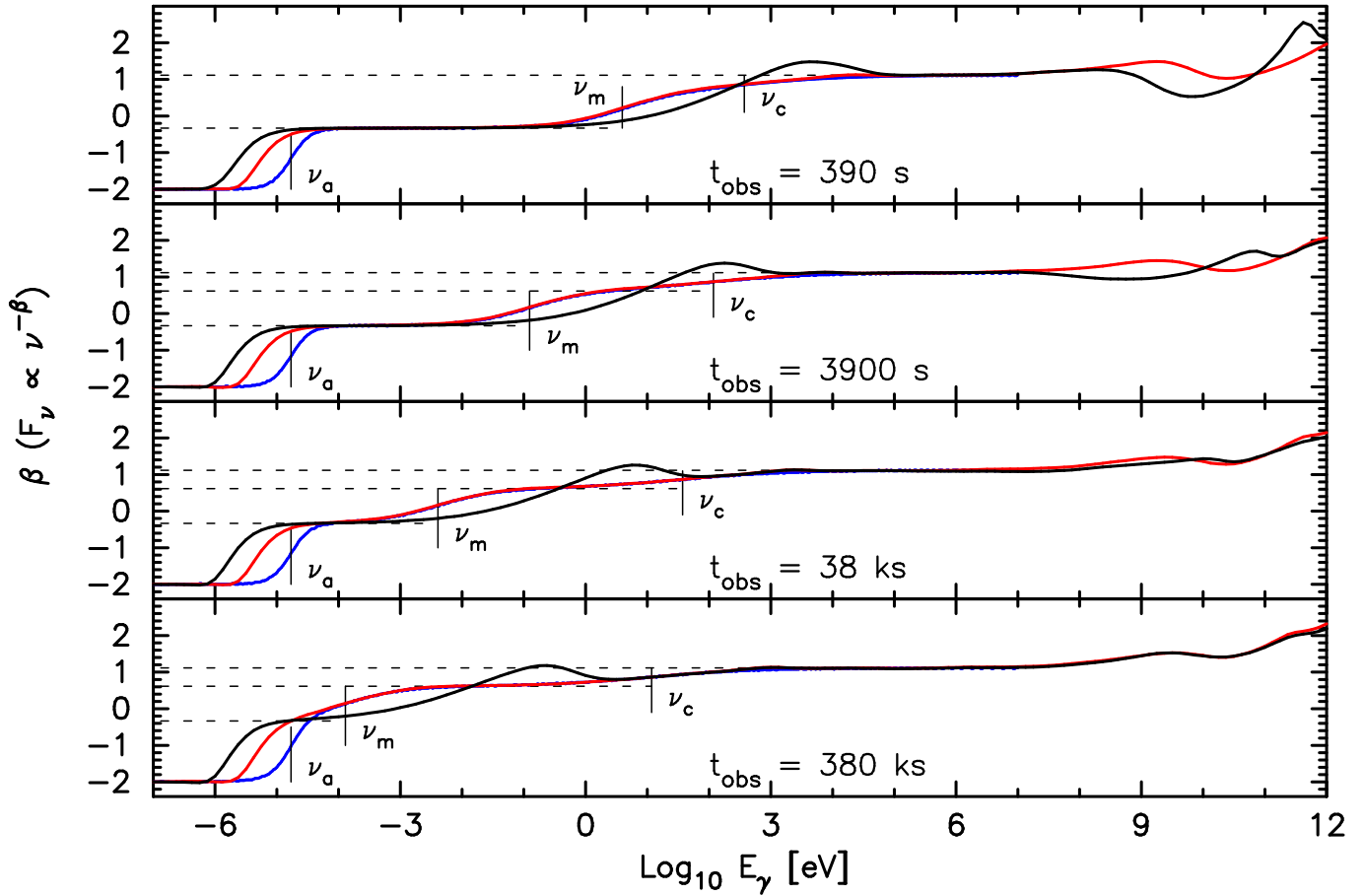


Figure 10. Spectral index of SEDs at four observer times. Blue curves are based on the fitting formulae of Granot & Sari (2002), red curves are based on the PPL model, and black curves are based on the ThPL model. As in Figure 13, we have identified the three spectral breaks associated with a slow-cooling afterglow (Granot & Sari 2002). We have also drawn horizontal guide lines for spectral regions associated with the traditional analytical afterglow model. In the top panel, these are drawn at $F_\nu \propto \nu^{1/3}$ and $F_\nu \propto \nu^{-p/2}$; in the bottom panels, they are drawn at $F_\nu \propto \nu^{1/3}$, $F_\nu \propto \nu^{(1-p)/2}$, and $F_\nu \propto \nu^{-p/2}$. Note that the blue curve ends at $E_\gamma = 10$ MeV, since the Granot & Sari (2002) formulae do not include SSC.

477 We showed broadband SEDs for the afterglow in Figure 6, but it is also instructive to consider the spectral
 478 index β as a function of photon energy. We demonstrate this behavior in Figure 10 for four times during the
 479 afterglow. The break frequencies are marked in order to more easily distinguish spectral regions.

480 The curves based on the PPL model (red) are in excellent agreement with those computed using the
 481 fitting formulae of Granot & Sari (2002) (blue). The largest difference is around the SSA break, seen also in
 482 Figure 13 and explained by our use of Equation 23 rather than their Equation (A20). The SSA break for the
 483 ThPL model (in black) is lower still than that of the PPL model (this was visible in Figure 4, but difficult to
 484 discern). This is a difference from (Warren et al. 2018); in that previous work, it was implicitly assumed that
 485 the NT-only model consisted of electrons in a power law, and a second population (set by the local density)
 486 of non-radiating, non-absorbing electrons at much lower energies.

487 One can see that $\nu_m < \nu_c$ for all times, consistent with the earlier expectation (Figure 6) that the afterglow
 488 is in the slow-cooling regime. In the ThPL afterglow, on the other hand, the thermal synchrotron peak is

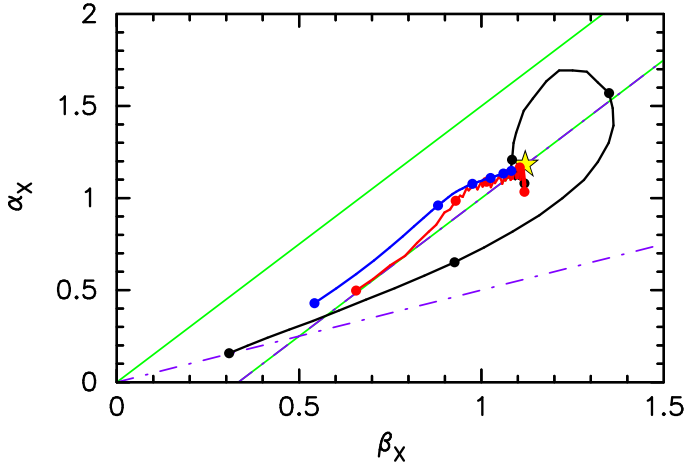


Figure 11. Tracks of α and β (in the 0.3 – 10 keV energy range) from $t_{\text{obs}} = 10$ s to $t_{\text{obs}} = 10^6$ s. All tracks begin around $\beta_X \approx 0.5$ and track up and to the right as time passes. Black is the ThPL model, red is the PPL model, and blue is derived from the fitting formulae of Granot & Sari (2002). The thin, purple, dash-dotted lines are the predicted closure relations for a GRB afterglow in the fast cooling regime, propagating into a constant-density medium; thin, green, solid lines are the same, but for the slow-cooling regime. Dots mark $t_{\text{obs}} = 10^1$ s, 10^2 s, 10^3 s, etc.; the yellow star is the late-time prediction of Granot & Sari (2002) for a pure power law when SSC is ignored.

489 higher in frequency than ν_m . This disparity means the thermal electrons act to delay the transition between
 490 fast cooling and slow cooling; indeed, the broad thermal peak is still passing through ν_c at $t_{\text{obs}} \sim 1$ hr. Once
 491 the thermal peak is entirely below ν_c , all three models are in in good agreement for their high-energy spectral
 492 indices.

493 The impact of SSC is visible in the top two panels of Figure 10. At very early times, thermal-thermal SSC
 494 produces a much wider range of β than can be achieved with just a power law of electrons: the Comptonized
 495 echo of the thermal peak is responsible for the local minimum in the ThPL β curve (at $E_\gamma = 10$ GeV for
 496 $t_{\text{obs}} = 390$ s), and the echo of the exponential rollover in the thermal distribution is responsible for the local
 497 maximum in the curve (at $E_\gamma \approx 1$ TeV for $t_{\text{obs}} = 390$ s). At moderate values of t_{obs} the ThPL and PPL
 498 curves have similar values for β , but at different photon energies. Given the differences between the early-
 499 time curves in Figure 10, a sufficiently bright burst with good time and energy coverage above GeV provides
 500 a good opportunity to discriminate between the PPL and ThPL models.

501 The GeV-TeV values of β for the PPL model do not vary much with time: there is some curvature at a
 502 few GeV and a few tens of GeV, but the shape of the spectrum is almost stationary when the emission is
 503 produced by a pure power-law distribution. The ThPL model, on the other hand, sees substantial variation
 504 with time as the thermal-thermal SSC peak decays in prominence. Thus, while both models are capable of
 505 producing a TeV $\beta \approx 1.6$ as seen in GRB 180720B (Abdalla et al. 2019), only the ThPL model can reproduce
 506 the softening in β from 1 to 2 that was observed in GRB 190114C (MAGIC Collaboration et al. 2019).

507

6. CLOSURE RELATIONS

508 Having discussed α and β separately in Section 5, we now restrict our focus to the *Swift* XRT range
 509 (0.3 – 10 keV) and plot them both together in Figure 11. This presentation allows for comparison between

our models and the closure relations that are frequently employed to interpret X-ray afterglows (Sari et al. 1998; Zhang & Mészáros 2004; Racusin et al. 2009; Srinivasaragavan et al. 2020).

The four straight lines in Figure 11 trace the predicted relations between α and β for a standard synchrotron afterglow, with $k = 0$ and $p > 2$. In both the slow-cooling regime (solid green) and the fast-cooling regime (dash-dotted purple), we show a pair of lines. One green line corresponds to the $\nu_m < \nu < \nu_c$ part of the SED, and the other line corresponds to the $\nu_c < \nu$ part of the SED (the same statements apply to the fast-cooling regime with ν_m and ν_c flipped). Observed photons must be (1) below the spectral break, (2) above the spectral break, or (3) in the transition region between the two. Thus the observed α and β must fall in the region bounded by the two lines.

The goal in this paper is not to determine which closure relations our afterglows satisfy, in order to diagnose the unknown conditions of an observed GRB. Instead we are comparing our afterglows to exactly those relations the standard synchrotron model predicts they should satisfy. We have marked with a star the late-time prediction of Figure 1 in Granot & Sari (2002). There is some early disagreement between the analytical points and the PPL model, caused by the numerical artifact discussed in Figure 14 of Appendix A. All three models (PPL model, ThPL model, and even the fitting formulae) converge on the same point in $\alpha - \beta$ space, but this point is not the one marked by the star.

While the PPL model and fitting formulae take similar tracks through Figure 11, the ThPL model takes a dramatically different path. Despite exactly the same GRB parameters as the PPL model, the ThPL model spends the early afterglow in the fast-cooling part of the $\alpha - \beta$ space. As the thermal synchrotron peak (and in particular its exponential turnover before the shock-accelerated tail) passes through the X-ray band, both α_X and β_X increase far beyond the range allowed by a pure power-law electron distribution. Once the thermal peak is below X-ray energies, those photons are produced by the nonthermal tail of the ThPL distributions, meaning the $\alpha - \beta$ track moves back towards those of the PPL model and fitting formulae. At very late times, both the PPL and ThPL models are impacted by SSC emission, which causes a slight drop in their α_X values. Given sufficient temporal coverage of a sufficiently bright GRB, it may be possible to produce such tracks and directly test for the shape associated with thermal electrons.

What is the maximum value that α_X or β_X may take? The peak values in Figure 11 were produced by the exponential tail of the thermal distribution, so varying f_{NT} —which impacts the height of the thermal peak relative to the power-law tail—should affect the $\alpha - \beta$ track taken by the afterglow. This is indeed the behavior seen in Figure 12.

- When f_{NT} is increased from the fiducial value of 1.9×10^{-2} , the ThPL tracks become more monotonic. This is sensible, as the electron distribution when f_{NT} is large has no obvious thermal peak: instead it resembles a smoothly-broken power law with a low-energy index of 2 (see Figure 15 in Appendix C). As visible in Figure 12, the tracks for large f_{NT} are monotonic, as is the track associated with the Granot & Sari (2002) fitting formulae. There is, however, a slight difference between the tracks of the two models. The fitting formulae track is “concave down”, where α_X increases more slowly than β_X does. ThPL tracks with large f_{NT} can instead be “concave up”, where β_X increases more slowly than does α_X . Despite the differences between the tracks, it may be impractical to make observations with enough precision to clearly distinguish the two possibilities should f_{NT} take large values.

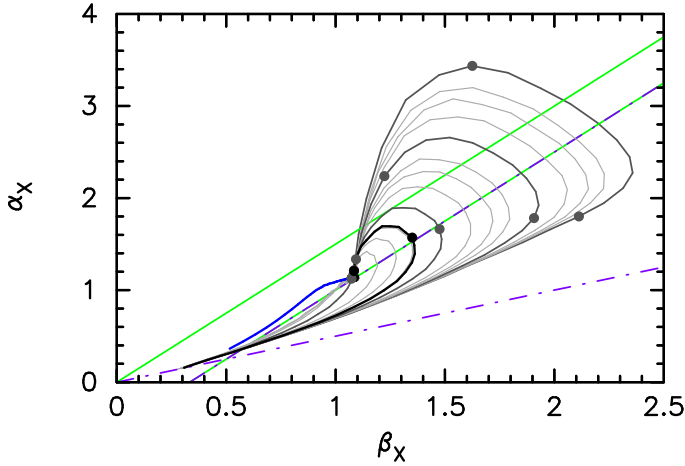


Figure 12. Largely the same as Figure 11, but with two changes. First, time runs from 10 s to 10^5 s since later behavior is not relevant here. Second, we compare only the ThPL model (black and gray curves) to the fitting formulae of Granot & Sari (2002) (blue curve), omitting the PPL model. Gray curves show impact of varying f_{NT} in the ThPL model. Thicker, dark gray curves show the tracks when $f_{\text{NT}} \in \{10^{-1}, 10^{-2}, 10^{-3}, 10^{-4}\}$; thinner, light gray curves represent $f_{\text{NT}} \in \{2, 3, 5\} \times \{10^{-1}, 10^{-2}, 10^{-3}, 10^{-4}\}$. The ThPL track and the dark gray tracks all have two observer times marked; proceeding counterclockwise from the bottom left corner, the first dot is $t_{\text{obs}} = 10^3$ s and the second is $t_{\text{obs}} = 10^4$ s.

- 549 • When f_{NT} is decreased from the fiducial value, the afterglow tracks have three distinct phases. In the
550 first phase, both α_X and β_X increase in the fast-cooling part of the space. The second phase begins
551 when the afterglow reaches its maximum value of β_X , and is marked by decreasing β_X and increasing
552 α_X . Finally, once the peak value of α_X is reached, the third phase occurs. This phase is characterized
553 by a rapid decline in α_X accompanied by a slower decline in (or an almost constant) β_X . The late-time
554 behavior, regardless of the value of f_{NT} , is the same point reached by all afterglows considered in
555 this work. We wish to emphasize that the afterglow is demonstrably in the slow-cooling regime at all
556 observer times considered (Figure 6), so these transitions are not due to a change in cooling: they are
557 directly due to the presence of thermal electrons in the distribution.
- 558 • For $f_{\text{NT}} < 0.01$, the track passes through both the fast-cooling and the slow-cooling regions in the
559 $\alpha - \beta$ plane, and still further into a region that does not satisfy either closure relation. Observations
560 of GRBs in this part of the space would signal not only the presence of thermal electrons, but that the
561 nonthermal part of the electron distribution is a small fraction of the overall population.
- 562 • The peak values of both α_X and β_X increase as f_{NT} decreases. For exactly the same GRB parameters,
563 inefficient injection into the shock-acceleration process (i.e. a pronounced thermal peak) allows α_X to
564 exceed 3, and for β_X to exceed 2, even though $p = 2.23$ for all the tracks shown in Figure 12.
- 565 • Not only do the extreme values of α_X and β_X increase when f_{NT} is reduced, but the track evolves
566 more slowly with time. The two sets of dots in Figure 12 show the positions of the tracks at observer
567 times of 10^3 s and 10^4 s. The fiducial model, with $f_{\text{NT}} = 1.9 \times 10^{-2}$, is crossing over from the fast-
568 cooling region to the slow-cooling region at $t_{\text{obs}} = 10^3$ s; by 10^4 s it has already reached agreement
569 with the fitting formulae. In contrast, when $f_{\text{NT}} = 10^{-4}$, the afterglow at $t_{\text{obs}} = 10^3$ s has yet to reach

its maximum value of β (and is still firmly in the fast-cooling part of the figure); and it has only just reached maximum α at 10^4 s.

- The afterglows modeled here correspond to Phase III of the canonical afterglow (Zhang et al. 2006; Racusin et al. 2009). Figure 2 of Racusin et al. (2009) presents a histogram of the α_X and β_X values of *Swift* afterglows observed during Phase III. The values of β_X cluster around 1.2, with a large but symmetric spread. The values of α_X , on the other hand, have a peak around 1.2 but a significant one-sided tail extending to $\alpha_X \approx 3$. As already mentioned above—and as visible in Figure 12—our simulated afterglows show just this behavior at late times. (While it is possible that selection effects can bias observations of α_X and β_X , a plot of GRB fluence versus α_X and β_X showed no clustering of the data, or a particular trend toward bright or faint bursts. We conclude that there is no clear selection bias causing the distribution of α_X and β_X presented in Racusin et al. (2009).)

7. CONCLUSIONS

This work presented a semi-analytical model for GRB afterglows including both thermal electrons and SSC photon production. Our main results are the following:

- We have extended the work of Granot & Sari (2002) and Ressler & Laskar (2017) by including a physically-motivated prescription for both the thermal distribution and the maximum electron energy. We are also including SSC for the first time in the context of thermal electrons, allowing us to calculate emission across every observable frequency range.
- Thermal particles affect the entirety of the afterglow, from GHz to TeV (Figures 4, 5, and 8). For our fiducial parameters, early-time TeV emission is boosted by more than order of magnitude when thermal particles are included; at late times the ThPL and PPL scenarios predict similar TeV production. Additionally, X-ray, optical, and radio light curves are all different between the ThPL and PPL scenarios, despite using the same fiducial parameters and the same normalizations for the respective electron distributions (both the overall normalization and that of the accelerated tail).
- For the GRB parameters we chose, the Compton Y parameter is much less than 1 for entire simulated afterglow (Figure 7). This parameter is likely to vary locally within the shocked region, and is sure to depend globally on the GRB parameters. For at least some of the relevant GRB parameter space, though, we retroactively justify our decision to ignore SSC cooling as a contributor to the maximum electron energy.
- Thermal electrons impact both temporal decay index α and spectral decay index β of emission. The most basic prediction, and one made previously in the literature (Giannios & Spitkovsky 2009; Warren et al. 2017), is non-monotonic evolution of α and β with time. We recover that result in the X-ray band (Figure 9), and examination of light curves suggests that a similar behavior happens at any frequency of interest (Figure 8).
- In the TeV band specifically, the ThPL model demonstrates changes in β with time (Figure 10). This is in stark contrast to the PPL model, which predicts no changes in β , and readily explains observations of TeV afterglows where the spectral index evolved with time.

- 607 • Closure relations are a common tool for interpreting afterglow observations. The ThPL and PPL
608 afterglows take very different paths through $\alpha - \beta$ space in X-ray (Figures 11, 12). In particular,
609 if $f_{\text{NT}} < 0.01$ then the ThPL track goes outside both the fast- and slow-cooling closure relations
610 (despite the fact that there is no third possibility in the standard synchrotron afterglow). Late time
611 X-ray behavior in the ThPL model (with $f_{\text{NT}} < 0.01$)—but not in the PPL model—is consistent with
612 Phase III afterglows as presented in [Racusin et al. \(2009\)](#).
- 613 • As pointed out in previous work, f_{NT} is a mostly free parameter (though PIC simulations suggest
614 should be in range of 1 – 3%). Curiously, making the canonical assumption (and one not based on a
615 physical justification) that the power-law part of the ThPL model overlaps with the PPL model causes
616 f_{NT} to match PIC predictions for the physically relevant range $2.2 \lesssim p \lesssim 2.5$. This is, as far as we can
617 tell, a numerical coincidence rather than signaling a deeper physical meaning.

618 Although we have presented here the most complete treatment to date of thermal electrons in GRB
619 afterglows, there are still numerous extensions and refinements that can be made to the model. An early
620 coasting phase ([Meszaros et al. 1993](#); [Kobayashi et al. 1999](#)) and energy injection ([Dai & Lu 1998](#); [Zhang &](#)
621 [Mészáros 2001](#)) may become observationally relevant if the ratio $E_{\text{iso}}/n_{\text{ext}}$ is greater than what was assumed
622 here. Although we assumed a spherically-symmetric blast wave, all available evidence points to GRB jets
623 having angular structure ([Lipunov et al. 2001](#); [Rossi et al. 2002](#); [Ito et al. 2019](#); [Gottlieb et al. 2021](#)). Given
624 that jets indeed have angular structure, the viewing angle is likely to lie off the jet axis, breaking the circular
625 symmetry and introducing further complications ([Granot et al. 2002](#); [Ryan et al. 2015, 2020](#)). It has also
626 been suggested that a significant portion of observed emission is produced by electrons ahead of the blast
627 wave ([Sironi & Spitkovsky 2009](#); [Sironi et al. 2015](#); [Derishev & Piran 2016, 2021](#)), though the anisotropic
628 nature of the magnetic field there makes computing emission more challenging. Finally, and perhaps most
629 obviously, the simulated afterglows here assumed a constant-density ambient medium. Using $k = 2$ rather
630 than $k = 0$ will affect the hydrodynamic evolution of the blast wave, and in turn the structure and evolution
631 of the SEDs. Any, or all, of these topics are worth exploring in future papers.

632 APPENDIX

633 A. VERIFICATION OF NUMERICAL CODE

634 As a test of the procedure outlined in Section 2, we compare it against two realizations of the standard
635 synchrotron afterglow. All three approaches used the GRB parameters listed in Table 2. In Figure 13 we
636 show spectral energy distributions (SEDs) for an early and a late observer time. The blue curves were pro-
637 duced using the fitting formulae of [Granot & Sari \(2002\)](#)—that is, their Table 2 and Eq. (5). The fitting
638 formulae are in good agreement with the SEDs computed using the full radiative transfer integral (Equa-
639 tion (A24) in that paper), shown in red in Figure 13; indeed, the two colors overlap almost perfectly for
640 most of the SEDs shown. The final pair of curves drawn in Figure 13 was computed using the PPL model
641 described in Section 2 (black lines). To better compare outputs, it was assumed that the non-thermal tail

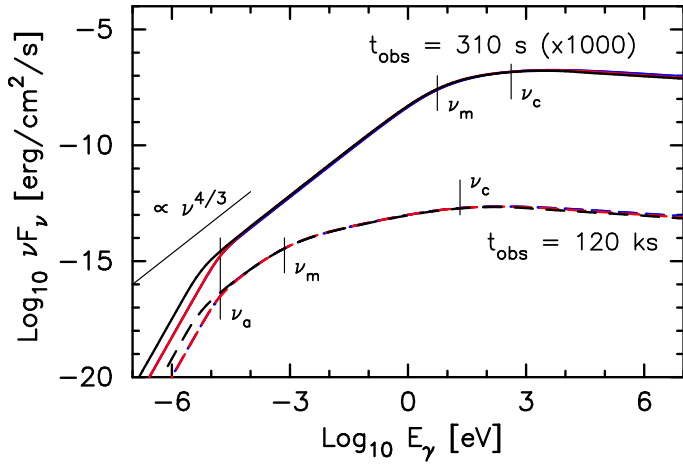


Figure 13. SEDs at two observer times for three different methods of computing afterglow emission. Solid lines show the SEDs for an observer time of 310 s (scaled by a factor of 1000 for clarity), and dashed lines show the SEDs for an observer time of 120 ks. Blue lines were computed using Table 2 and Eq. (5) from [Granot & Sari \(2002\)](#); red lines were computed using Eq. (A24) of that paper; and black lines use the PPL model outlined in Section 2. The three spectral breaks associated with a slow-cooling afterglow (absorption, injection, and cooling) are also identified.

642 extended to arbitrarily high energies (rather than ending where radiative losses exceed acceleration gains, as
643 in Equation 10).

644 For ease of comprehension, we have identified the key break frequencies in Figure 13. Since $\nu_m < \nu_c$ for
645 both times shown, the afterglow is in the slow-cooling regime. As pointed out in Equation 34, the transition
646 from fast to slow cooling happens extremely early for the GRB parameters used, so this ordering of break
647 frequencies is to be expected.

648 The three computing methods agree quite well for most of the energy range shown in Figure 13. The
649 most obvious difference is at the low end of the SEDs: specifically, the location of ν_a , at which the afterglow
650 becomes optically thick. The black curve in Figure 13 predicts an absorption frequency notably lower than do
651 the two methods presented in [Granot & Sari \(2002\)](#), due to our use of Equation 23 rather than Equation (A20)
652 in the latter paper.

653 Beyond the significant difference at low energies, there is also slight disagreement at high photon
654 energies—on the order of 10 – 15%—which persists regardless of the integration method implemented
655 or the fineness of the various discretizations used (photon energy, angular integration, radiative transfer in-
656 tegration). Inspection of Figure 14 reveals the reason for this discrepancy. This figure shows the spectral
657 index β as a function of photon energy for the same energy range as Figure 13. It can be seen that the blue
658 curves (based on the fitting formulae in [Granot & Sari 2002](#)) smoothly vary in the vicinity of ν_c , as indeed
659 they are mathematically required to do. As the cooling break transitions into the highest-energy power-law
660 segment (PLS H in Figure 1 of [Granot & Sari 2002](#)), the two numerical integrators (in red and black) behave
661 differently. Rather than a smooth transition to the eventual value of β , they continue to increase more steeply,
662 and even slightly overshoot the endpoint before relaxing back to it. This larger value of β means their SEDs
663 decline more rapidly than the SED of the fitting formulae, which causes the slight disparity at high photon
664 energies in Figure 13.

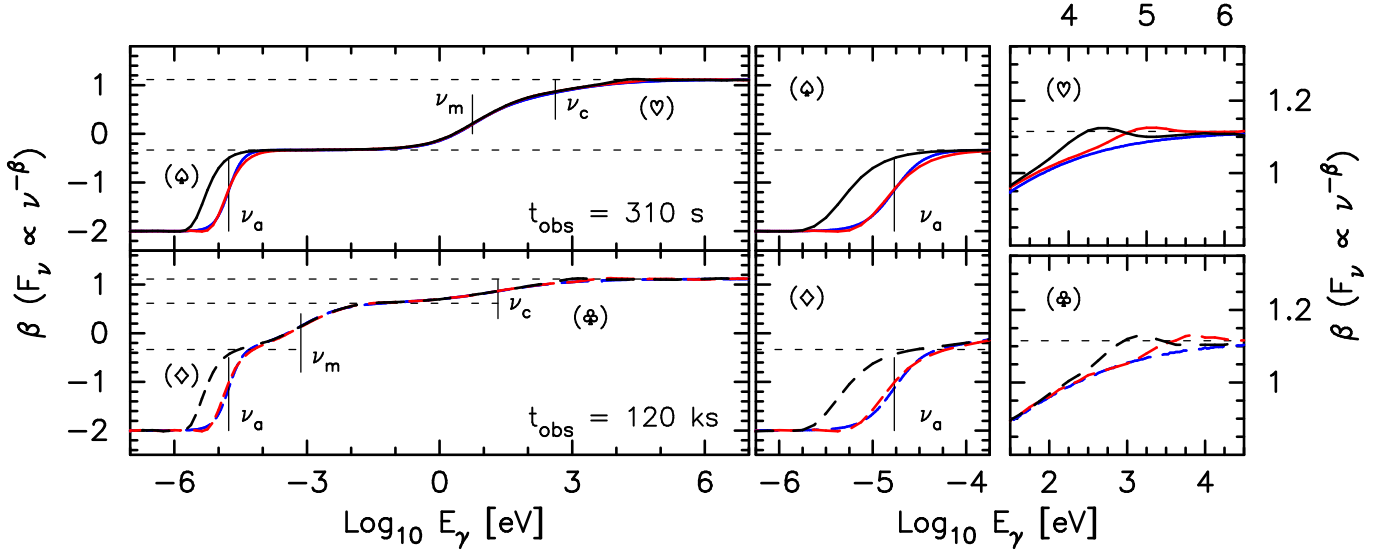


Figure 14. Spectral index of SEDs at two observer times. Colors and line types are as in Figure 13. As in Figure 13, we have identified the three spectral breaks associated with a slow-cooling afterglow in Granot & Sari (2002). We have also drawn horizontal guide lines for spectral regions associated with the traditional analytical afterglow model. In the top panel, these are drawn at $F_\nu \propto \nu^{1/3}$ and $F_\nu \propto \nu^{-p/2}$; in the bottom panel, they are drawn at $F_\nu \propto \nu^{1/3}$, $F_\nu \propto \nu^{(1-p)/2}$, and $F_\nu \propto \nu^{-p/2}$. In the left two panels, we have identified four locations with the symbols \heartsuit , \diamond , \circledast , and \heartsuit . The right four panels expand the region identified by each symbol, to more clearly show the differences between each set of curves.

665 The key result from Figures 13 and 14 is that our code correctly reproduces the key spectral features and
 666 temporal behavior of the fitting formulae in Granot & Sari (2002). The slight discrepancy around ν_c appears
 667 to be numerical in nature rather than physical. As it seems to behave in a consistent manner regardless
 668 of observer time, it could be corrected during or after the calculation should percent-level accuracy ever
 669 become necessary.

670 B. THE SYNCHROTRON ABSORPTION COEFFICIENT α_ν

671 In order to compute synchrotron self-absorption, we employed Equation (6.50) of Rybicki & Lightman
 672 (1979) (Equation 23 here). A different form of the equation is used in Granot & Sari (2002). In a footnote
 673 in that paper, those authors state that “eq. (18) of Granot et al. (1999b), which is essentially eq. (6.52) of
 674 Rybicki & Lightman (1979), misses the term associated with the discontinuity at the lower edge of the
 675 electron distribution (at γ_{\min}) when derived from eq. (6.50) of Rybicki & Lightman. This missing term
 676 caused an overestimation of the absorption coefficient by a factor of $f = 3(p + 2)/4$ ”.

677 The alternate equation is found in Appendix A of that paper:

$$\alpha_{\nu, \text{GS}} = \frac{1}{8\pi m \nu^2} \int_{\gamma_{\min}}^{\gamma_{\max}} \frac{N(\gamma)}{\gamma^2} \frac{\partial}{\partial \gamma} [\gamma^2 P(\nu, \gamma)] d\gamma \quad (\text{B1})$$

678 Note that the equation involves the derivative of $P(\nu, \gamma)$ rather than of $N(\gamma)$ ($= dn_\gamma/d\gamma$) as in Equation (6.50)
 679 of Rybicki & Lightman (1979). The two equations are linked through integration by parts:

$$\alpha_{\nu, \text{GS}} = -\frac{1}{8\pi m \nu^2} \int_{\gamma_{\min}}^{\gamma_{\max}} \gamma^2 P(\nu, \gamma) \frac{\partial}{\partial \gamma} \left[\frac{N(\gamma)}{\gamma^2} \right] d\gamma + \frac{1}{8\pi m \nu^2} [N(\gamma)P(\nu, \gamma)]_{\gamma_{\min}}^{\gamma_{\max}} \quad (\text{B2})$$

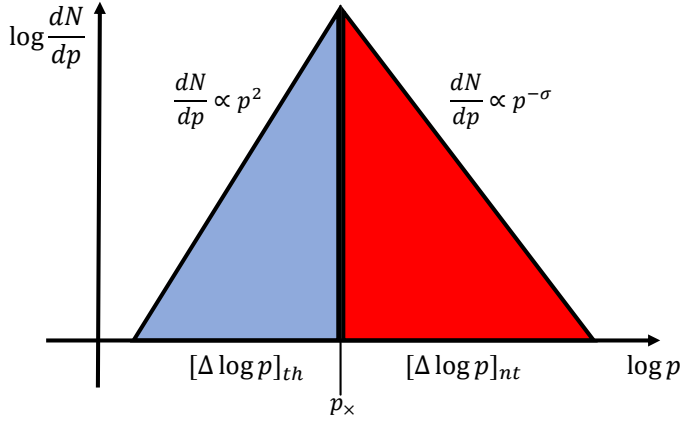


Figure 15. Illustration of a scenario leading to the maximum possible value of f_{NT} . Note that we use momentum (rather than energy or Lorentz factor) as our dependent variable. To avoid using the same symbol twice for different quantities, we therefore refer to the non-thermal spectral index as σ here rather than as p (which it is called elsewhere in this paper).

680 The first term in Equation B2 is simply Equation 23, while the second term contains information about the
 681 endpoints of the distribution.

682 Let us assume that $\gamma_{\text{max}} \rightarrow \infty$, and that we are dealing with a power-law distribution of electrons, $N(\gamma) =$
 683 $K_{\text{pl}}\gamma^{-p}$, whose index $p > 2$. Then the γ_{max} endpoint term vanishes (since $N(\gamma_{\text{max}}) \rightarrow 0$), and Equation B2
 684 may be rewritten

$$\begin{aligned}
 \alpha_{v,\text{GS}} &= \Omega n \frac{3(p-1)(p+2)}{3p+2} \gamma_{\text{min}}^{-5/3} - \Omega K_{\text{pl}} \gamma_{\text{min}}^{-p-\frac{2}{3}} \\
 &= \Omega n \frac{3(p-1)(p+2)}{3p+2} \gamma_{\text{min}}^{-5/3} - \Omega n (p-1) \gamma_{\text{min}}^{-5/3} \\
 &= \Omega n \frac{4(p-1)}{3p+2} \gamma_{\text{min}}^{-5/3}.
 \end{aligned} \tag{B3}$$

685 In the above equation we have assumed that $P(v, \gamma)$ lies in the $v^{1/3}$ part of the spectrum, and we have collected
 686 numerical prefactors into the single term Ω for easier readability; the substitution $K_{\text{pl}} = n(p-1)\gamma_{\text{min}}^{p-1}$ comes
 687 from the normalization condition $\int N d\gamma = n$ for a desired number density n .

688 Repeating the above exercise for Equation 23 leads to (Warren et al. 2018)

$$\alpha_{v,\text{RL}} = \Omega n \frac{3(p-1)(p+2)}{3p+2} \gamma_{\text{min}}^{-5/3}, \tag{B4}$$

689 which is greater by a factor $3(p+2)/4$ than the end result of Equation B3. We therefore use Equation 23 to
 690 compute the absorption coefficient rather than Equation B1.

691 C. MAXIMUM f_{NT} WITH A “THERMAL” DISTRIBUTION

692 For a thermal distribution, the maximum value of f_{NT} occurs when p_x lies below the thermal peak
 693 completely, falling instead in the p^2 low-energy part of the distribution. Such a situation is illustrated in
 694 Figure 15, but note the different use of symbols here as opposed to the rest of this work: we use p to denote

695 electron momentum rather than a spectral index, and we instead use σ for the spectral index of the accelerated
696 electron population.

697 The thermal particle number can be calculated as

$$N_{th} = \int_0^{p_x} C p^2 dp = C \frac{p_x^3}{3} \quad (C5)$$

698 where C is a normalization constant. The number of non-thermal particles is

$$N_{nt} = \int_{p_x}^{\infty} C p_x^{2+\sigma} p^{-\sigma} dp = C \frac{p_x^3}{\sigma - 1} \quad (C6)$$

699 with a normalization constant $C p_x^{2+\sigma}$ required so the two parts of the distribution meet at p_x . Thus

$$\begin{aligned} f_{NT,max} &= \frac{N_{nt}}{N_{nt} + N_{th}} \\ &= \frac{3}{\sigma + 2}, \end{aligned} \quad (C7)$$

700 precisely the formula recovered from Equation (17) of [Ressler & Laskar \(2017\)](#).

ACKNOWLEDGMENTS

This work was funded in part by the Interdisciplinary Theoretical and Mathematical Sciences (iTHEMS, <https://ithems.riken.jp>) program at RIKEN (DCW, SN). MB would like to acknowledge support by NASA grants 80NSSC17K0757 and NNH19ZDA001N-FERMI, and NSF grants 10001562 and 10001521. This work is supported by JSPS Grants-in-Aid for Scientific Research ‘‘KAKENHI’’ (A: Grant Number JP19H00693). SN also acknowledges the support from Pioneering Program of RIKEN for Evolution of Matter in the Universe (r-EMU). BA acknowledges support from the Swedish Research Council (grant reference number 2020-00540). HI acknowledges support from JSPS KAKENHI Grant Number JP19K03878 and JP20H04751.

REFERENCES

- | | | | |
|-----|---|-----|---|
| 701 | Abdalla, H., Adam, R., Aharonian, F., et al. 2019, | 710 | Böttcher, M. & Dermer, C. D. 1998, The Astrophysical |
| 702 | Nature, 575, 464 | 711 | Journal Letters, 499, L131 |
| 703 | Barkov, M. V., Luo, Y., & Lyutikov, M. 2021, | 712 | Costa, E., Frontera, F., Heise, J., et al. 1997, Nature, |
| 704 | Astrophysical Journal, 907, 109 | 713 | 387, 783 |
| 705 | Blandford, R. D. & McKee, C. F. 1976, Physics of | 714 | Dai, Z. G. & Lu, T. 1998, MNRAS, 298, 87 |
| 706 | Fluids, 19, 1130 | 715 | Dainotti, M. G., Lenart, A. Ł., Fraija, N., et al. 2021a, |
| 707 | Bloom, J. S., Djorgovski, S. G., Kulkarni, S. R., & | 716 | PASJ |
| 708 | Frail, D. A. 1998, The Astrophysical Journal Letters, | 717 | Dainotti, M. G., Omodei, N., Srinivasaragavan, G. P., |
| 709 | 507, L25 | 718 | et al. 2021b, ApJS, 255, 13 |

- 719 Derishev, E. & Piran, T. 2019, *The Astrophysical*
720 *Journal Letters*, 880, L27
- 721 Derishev, E. & Piran, T. 2021, arXiv e-prints,
722 arXiv:2106.12035
- 723 Derishev, E. V. & Piran, T. 2016, *MNRAS*, 460, 2036
- 724 Eichler, D. & Waxman, E. 2005, *Astrophysical*
725 *Journal*, 627, 861
- 726 Ellison, D. C. 1985, *Journal of Geophysical Research*,
727 90, 29
- 728 Ellison, D. C., Warren, D. C., & Bykov, A. M. 2013,
729 *Astrophysical Journal*, 776, 46
- 730 Fraija, N., Barniol Duran, R., Dichiarà, S., &
731 Beniamini, P. 2019, *Astrophysical Journal*, 883, 162
- 732 Gao, H., Lei, W.-H., Zou, Y.-C., Wu, X.-F., & Zhang,
733 B. 2013, *New Astronomy Reviews*, 57, 141
- 734 Giannios, D. & Spitkovsky, A. 2009, *MNRAS*, 400,
735 330
- 736 Gottlieb, O., Nakar, E., & Bromberg, O. 2021,
737 *MNRAS*, 500, 3511
- 738 Granot, J., Panaitescu, A., Kumar, P., & Woosley, S. E.
739 2002, *The Astrophysical Journal Letters*, 570, L61
- 740 Granot, J., Piran, T., & Sari, R. 1999a, *Astrophysical*
741 *Journal*, 513, 679
- 742 Granot, J., Piran, T., & Sari, R. 1999b, *Astrophysical*
743 *Journal*, 527, 236
- 744 Granot, J. & Sari, R. 2002, *Astrophysical Journal*, 568,
745 820
- 746 Ito, H., Matsumoto, J., Nagataki, S., et al. 2019, *Nature*
747 *Communications*, 10, 1504
- 748 Japelj, J., Kopač, D., Kobayashi, S., et al. 2014,
749 *Astrophysical Journal*, 785, 84
- 750 Jones, F. C. 1968, *Physical Review*, 167, 1159
- 751 Kafexhiu, E., Aharonian, F., & Barkov, M. 2019,
752 *PhRvD*, 99, 063007
- 753 Kobayashi, S., Piran, T., & Sari, R. 1999,
754 *Astrophysical Journal*, 513, 669
- 755 Laskar, T., Alexander, K. D., Berger, E., et al. 2016,
756 *Astrophysical Journal*, 833, 88
- 757 Lemoine, M. 2013, *MNRAS*, 428, 845
- 758 Lemoine, M., Li, Z., & Wang, X.-Y. 2013, *MNRAS*,
759 435, 3009
- 760 Lemoine, M. & Pelletier, G. 2011, *MNRAS*, 417, 1148
- 761 Lipunov, V. M., Postnov, K. A., & Prokhorov, M. E.
762 2001, *Astronomy Reports*, 45, 236
- 763 Liu, R.-Y., Wang, X.-Y., & Wu, X.-F. 2013, *The*
764 *Astrophysical Journal Letters*, 773, L20
- 765 MAGIC Collaboration, Acciari, V. A., Ansoldi, S.,
766 et al. 2019, *Nature*, 575, 459
- 767 Meszaros, P., Laguna, P., & Rees, M. J. 1993,
768 *Astrophysical Journal*, 415, 181
- 769 Meszaros, P., Rees, M. J., & Pathanassiou, H. 1994,
770 *Astrophysical Journal*, 432, 181
- 771 Metzger, M. R., Djorgovski, S. G., Kulkarni, S. R.,
772 et al. 1997, *Nature*, 387, 878
- 773 Nousek, J. A., Kouveliotou, C., Grupe, D., et al. 2006,
774 *Astrophysical Journal*, 642, 389
- 775 Paczyński, B. & Rhoads, J. E. 1993, *The Astrophysical*
776 *Journal Letters*, 418, L5
- 777 Perley, D. A., Cenko, S. B., Corsi, A., et al. 2014,
778 *Astrophysical Journal*, 781, 37
- 779 Planck Collaboration, Aghanim, N., Akrami, Y., et al.
780 2020, *Astronomy and Astrophysics*, 641, A6
- 781 Racusin, J. L., Liang, E. W., Burrows, D. N., et al.
782 2009, *Astrophysical Journal*, 698, 43
- 783 Ressler, S. M. & Laskar, T. 2017, *Astrophysical*
784 *Journal*, 845, 150
- 785 Rossi, E., Lazzati, D., & Rees, M. J. 2002, *MNRAS*,
786 332, 945
- 787 Ryan, G., van Eerten, H., MacFadyen, A., & Zhang,
788 B.-B. 2015, *Astrophysical Journal*, 799, 3
- 789 Ryan, G., van Eerten, H., Piro, L., & Troja, E. 2020,
790 *Astrophysical Journal*, 896, 166
- 791 Rybicki, G. B. & Lightman, A. P. 1979, *Radiative*
792 *processes in astrophysics* (Wiley)
- 793 Sari, R. & Esin, A. A. 2001, *Astrophysical Journal*,
794 548, 787
- 795 Sari, R., Piran, T., & Narayan, R. 1998, *The*
796 *Astrophysical Journal Letters*, 497, L17
- 797 Sironi, L., Keshet, U., & Lemoine, M. 2015, *Space*
798 *Science Reviews*, 191, 519
- 799 Sironi, L. & Spitkovsky, A. 2009, *The Astrophysical*
800 *Journal Letters*, 707, L92
- 801 Sironi, L. & Spitkovsky, A. 2011, *Astrophysical*
802 *Journal*, 726, 75
- 803 Sironi, L., Spitkovsky, A., & Arons, J. 2013,
804 *Astrophysical Journal*, 771, 54
- 805 Srinivasaragavan, G. P., Dainotti, M. G., Fraija, N.,
806 et al. 2020, *Astrophysical Journal*, 903, 18
- 807 Toma, K., Ioka, K., & Nakamura, T. 2008, *The*
808 *Astrophysical Journal Letters*, 673, L123
- 809 Troja, E., van Eerten, H., Ryan, G., et al. 2019,
810 *MNRAS*, 489, 1919
- 811 van Paradijs, J., Groot, P. J., Galama, T., et al. 1997,
812 *Nature*, 386, 686
- 813 Wang, X.-Y., Liu, R.-Y., Zhang, H.-M., Xi, S.-Q., &
814 Zhang, B. 2019, *Astrophysical Journal*, 884, 117

- 815 Warren, D. C., Barkov, M. V., Ito, H., Nagataki, S., &
816 Laskar, T. 2018, MNRAS, 480, 4060
- 817 Warren, D. C., Beauchemin, C. A. A., Barkov, M. V.,
818 & Nagataki, S. 2021, Astrophysical Journal, 906, 33
- 819 Warren, D. C., Ellison, D. C., Barkov, M. V., &
820 Nagataki, S. 2017, Astrophysical Journal, 835, 248
- 821 Warren, D. C., Ellison, D. C., Bykov, A. M., & Lee,
822 S.-H. 2015, MNRAS, 452, 431
- 823 Wright, E. L. 2006, Publications of the Astronomical
824 Society of the Pacific, 118, 1711
- 825 Zacharias, M. & Schlickeiser, R. 2013, Astrophysical
826 Journal, 777, 109
- 827 Zhang, B., Fan, Y. Z., Dyks, J., et al. 2006,
828 Astrophysical Journal, 642, 354
- 829 Zhang, B. & Kobayashi, S. 2005, Astrophysical
830 Journal, 628, 315
- 831 Zhang, B. & Mészáros, P. 2001, Astrophysical Journal,
832 559, 110
- 833 Zhang, B. & Mészáros, P. 2004, International Journal
834 of Modern Physics A, 19, 2385